


 Cite this: *RSC Adv.*, 2026, 16, 8051

Structure–luminescence correlations in Eu^{3+} -activated Ba_2LaVO_6 and Ba_2GdVO_6 double-perovskite phosphors

 Mustafa İlhan,^a Sibel Gökçe,^b Lütfiye Feray Güteryüz^d and Mehmet İsmail Katıç^c

Eu^{3+} -activated double perovskites have attracted increasing attention as red-emitting phosphors owing to their compositional tunability and structurally versatile host lattices. In this work, $\text{Ba}_2\text{La}_{1-x}\text{VO}_6:\text{xEu}^{3+}$ and $\text{Ba}_2\text{Gd}_{1-x}\text{VO}_6:\text{xEu}^{3+}$ ($x = 0$ and 2.5–30 mol%) phosphors were synthesized *via* a solid-state reaction route and systematically investigated to elucidate host-dependent luminescence behavior. X-ray diffraction combined with Rietveld refinement confirmed single-phase orthorhombic *Pnma* symmetry for both systems, with the La-based host exhibiting a more flexible and polarizable lattice, while the Gd-based host forms a more compact and rigid framework. Distinct host-dependent microstructural features are observed by scanning electron microscopy (SEM) for the La-based and Gd-based phosphors. X-ray photoelectron spectroscopy (XPS) was further employed to verify the elemental composition and the trivalent oxidation state of Eu ions in representative high-doping compositions. Photoluminescence studies reveal pronounced differences in emission characteristics: $\text{Ba}_2\text{LaVO}_6:\text{Eu}^{3+}$ stabilizes an abnormal near-UV-excited $^5\text{D}_0 \rightarrow ^7\text{F}_4$ -dominated orange-red emission with high dopant tolerance up to 30 mol% Eu^{3+} , whereas $\text{Ba}_2\text{GdVO}_6:\text{Eu}^{3+}$ exhibits the conventional $^5\text{D}_0 \rightarrow ^7\text{F}_2$ -dominated red emission with earlier concentration quenching beyond 15 mol%. Temperature-dependent photoluminescence measurements further reveal distinct thermal quenching behaviors, reflected in different quenching onsets and half-intensity temperatures ($T_{0.5}$), which are closely linked to the lattice rigidity of the two hosts. CIE analysis shows that $\text{Ba}_2\text{LaVO}_6:\text{Eu}^{3+}$ emits orange-red light with moderate color purity due to enhanced $^5\text{D}_0 \rightarrow ^7\text{F}_4$ emission, whereas $\text{Ba}_2\text{GdVO}_6:\text{Eu}^{3+}$ produces deeper red emission dominated by the $^5\text{D}_0 \rightarrow ^7\text{F}_2$ transition. Overall, this comparative study establishes a clear structure–rigidity–luminescence correlation in Eu^{3+} -activated Ba_2MVO_6 ($\text{M} = \text{La}, \text{Gd}$) phosphors, providing fundamental insight into host-controlled emission tuning in double-perovskite systems.

Received 25th November 2025

Accepted 30th January 2026

DOI: 10.1039/d5ra09112h

rsc.li/rsc-advances

1. Introduction

Rare-earth-doped phosphor materials have attracted considerable attention owing to their outstanding optical properties, including sharp emission lines, long lifetimes, high color purity, and robust chemical stability. Such features make them suitable for diverse applications in solid-state lighting, displays, lasers, bio-imaging, and security technologies.^{1–12} Among various activator ions, Eu^{3+} is especially important due to its strong red emission originating from the $^5\text{D}_0 \rightarrow ^7\text{F}_j$ ($j = 0–6$)

transitions, which are crucial for achieving warm-white or deep-red components in white light-emitting diodes (WLEDs).^{13–15}

In recent years, double perovskite-type oxides with the general formula $\text{A}_2\text{BB}'\text{O}_6$ have emerged as versatile host lattices for luminescent materials. Their wide band gaps, high structural stability, and compositional flexibility allow fine-tuning of both crystal and optical properties. In particular, substitutions at the A-site (alkaline-earth or rare-earth ions) and B/B'-sites (transition metal or rare-earth ions) provide a powerful means to modulate the local crystal field and energy transfer dynamics. Such structural adaptability renders double perovskites highly promising platforms for photonic applications.^{14–28} Within this family, vanadate-based double perovskites have drawn special interest because the VO_6 units can enhance excitation efficiency through charge-transfer transitions, while rare-earth ions at the A-site or B-site further tailor the optical behavior.^{25–28} In this context, although Eu^{3+} -doped vanadates have been extensively studied,^{29–33} investigations on Eu^{3+} -doped double perovskites remain scarce, with $\text{Ba}_2\text{GdVO}_6:\text{Eu}^{3+}$ reported only by Meng *et al.*²⁸ On the other hand, Gd^{3+} is well recognized as an efficient

^aDepartment of Jewelry and Jewelry Design, Faculty of Applied Sciences, Marmara University, Kartal, 34865, İstanbul, Türkiye. E-mail: mustafa.ilhan@marmara.edu.tr

^bDepartment of Physics, Faculty of Engineering and Natural Sciences, Manisa Celal Bayar University, Yunusemre, 45140, Kocaeli, Manisa, Türkiye

^cDepartment of Automotive Engineering, Faculty of Technology, Kocaeli University, İzmit, 41001, Kocaeli, Türkiye

^dDepartment of Medical Imaging Techniques, Vocational School of Health Sciences, Manisa Celal Bayar University, 45030, Manisa, Türkiye



sensitizer, transferring excitation energy to Eu^{3+} , whereas La^{3+} —with its larger ionic radius and more flexible coordination environment—induces greater lattice distortion and modifies the branching ratios of Eu^{3+} emissions. These contrasting roles highlight the importance of a comparative study between La-based and Gd-based hosts for understanding host-activator interactions. Notably, an unusual dominance of the ${}^5\text{D}_0 \rightarrow {}^7\text{F}_4$ transition has been reported in several La-based hosts; for example, Eu^{3+} -doped BaLaGaO_4 and Eu^{3+} -doped $\text{NaLa}_2\text{F}_3(\text{CN})_2$ exhibit anomalously intense ${}^5\text{D}_0 \rightarrow {}^7\text{F}_4$ emission,^{34,35} while (La, Mg)-substituted $\text{SrAl}_{12}\text{O}_{19}$ phosphors display pronounced ${}^5\text{D}_0 \rightarrow {}^7\text{F}_4$ photoluminescence under specific La/Mg ratios.³⁶ Such findings suggest unique site-selective excitation mechanisms and emphasize the need for detailed structural-optical correlation studies. Moreover, the influence of host lattice volume—larger for La^{3+} and smaller for Gd^{3+} —on concentration quenching, energy transfer, and thermal stability remains insufficiently clarified.

In this work, $\text{Ba}_2\text{La}_{1-x}\text{VO}_6:\text{xEu}^{3+}$ and $\text{Ba}_2\text{Gd}_{1-x}\text{VO}_6:\text{xEu}^{3+}$ ($x = 0\text{--}30$ mol%) phosphors were synthesized *via* a conventional solid-state reaction method and systematically investigated to establish a clear host-dependent structure-optical relationship. Their crystal structures were refined using X-ray diffraction (XRD) and Rietveld analysis, while scanning electron microscopy (SEM) was employed to examine the microstructural features. Comprehensive photoluminescence (PL), excitation (PLE), decay dynamics, and Judd-Ofelt analyses were performed to elucidate how the local lattice environments of La^{3+} and Gd^{3+} govern Eu^{3+} emission characteristics. In addition, X-ray photoelectron spectroscopy (XPS) was utilized to verify the elemental composition and oxidation state of Eu^{3+} ions in representative high-doping compositions. Distinct from most previously reported Eu^{3+} -activated double perovskites, the Ba_2LaVO_6 host stabilizes an abnormal ${}^5\text{D}_0 \rightarrow {}^7\text{F}_4$ -dominated deep-red emission and exhibits an unusually high Eu^{3+} solubility without severe concentration quenching up to 30 mol%, whereas Ba_2GdVO_6 shows conventional ${}^5\text{D}_0 \rightarrow {}^7\text{F}_2$ -dominated emission with earlier quenching. Furthermore, temperature-dependent PL measurements were carried out to correlate lattice rigidity with thermal quenching behavior and non-radiative activation energy. By directly comparing La-based and Gd-based hosts within the same vanadate double-perovskite framework, this study provides new insight into excitation-emission mechanism control and dopant-tolerant lattice design, offering practical guidelines for the development of high-performance red-emitting phosphors for photonic applications.

2. Experimental

$\text{Ba}_2\text{La}_{1-x}\text{VO}_6:\text{xEu}^{3+}$ and $\text{Ba}_2\text{Gd}_{1-x}\text{VO}_6:\text{xEu}^{3+}$ ($x = 0, 2.5, 5, 10, 15, 20,$ and 30 mol%) phosphor series were synthesized *via* a conventional solid-state reaction method. High-purity starting materials, including BaCO_3 (99%), La_2O_3 (99.99%), Gd_2O_3 (99.99%), V_2O_5 (99.9%) and Eu_2O_3 (99.9%) were used without further purification. Stoichiometric amounts corresponding to $\text{Ba}_2\text{M}_{1-x}\text{VO}_6:\text{xEu}^{3+}$ ($\text{M} = \text{La}, \text{Gd}$) compositions were accurately weighed and thoroughly mixed in an agate mortar to achieve

compositional homogeneity. The mixed powders were pressed into pellets and placed in alumina crucibles for sintering. The Eu^{3+} -doped Ba_2LaVO_6 and Ba_2GdVO_6 samples were calcined at 1350 °C and 1325 °C for 3 h, respectively, followed by natural cooling to room temperature.

Phase identification was performed using powder X-ray diffraction (XRD; D2 PHASER, Bruker Corp., Germany) with Cu K α radiation ($\lambda = 1.5406$ Å) over the 2θ range of $20\text{--}80^\circ$ at a scanning rate of 2°min^{-1} . Rietveld refinement was applied to extract lattice parameters and confirm phase purity. Microstructural features and grain morphology were examined using field-emission scanning electron microscopy (FE-SEM; XL 30S, Philips Corp., Netherlands). The elemental composition and chemical states of the samples were defined using X-ray photoelectron spectroscopy (XPS, Thermo Fisher Scientific Inc. U.S.) Al-K α (1486.6 eV). Photoluminescence (PL), photoluminescence excitation (PLE), and decay measurements were carried out using a fluorescence spectrometer (FS5, Edinburgh Instruments, UK) equipped with a 450 W ozone-free xenon lamp. Emission and excitation slit widths were kept constant during all measurements to ensure data consistency. For lifetime analysis, short microsecond excitation pulses were generated using pulsed xenon flash lamps (μF_1 and μF_2 , 5 W and 60 W), and decay signals were recorded using a time-correlated single-photon counting (TCSPC) module. Temperature-dependent PL analysis was conducted in the range of $300\text{--}550$ K using the FS5 spectrometer equipped with a controlled heating stage. Thermal activation energies (E_a) were extracted from Arrhenius fitting of the normalized emission intensity data. All photoluminescence measurements were repeated at least three times under identical experimental conditions to ensure reproducibility, and the reported trends represent averaged results. All optical characterizations were performed at room temperature.

3. Results and discussions

3.1 XRD, SEM and XPS results

The crystal structure and phase purity of the synthesized $\text{Ba}_2\text{La}_{1-x}\text{VO}_6:\text{xEu}^{3+}$ and $\text{Ba}_2\text{Gd}_{1-x}\text{VO}_6:\text{xEu}^{3+}$ ($x = 0, 2.5, 5, 10, 15, 20,$ and 30 mol%) samples were analyzed by powder X-ray diffraction (XRD) in the 2θ range of $10^\circ\text{--}80^\circ$, as shown in Fig. 1 and 2, respectively. The diffraction peaks of both series can be well indexed to the orthorhombic double-perovskite structure with space group $Pnma$, in good agreement with the standard JCPDS card No. 48-1036 reported for Ba_2GdVO_6 ,²⁸ confirming that the target phase was successfully formed without detectable secondary phases within the sensitivity of the instrument. Importantly, no significant peak shifts or additional impurity reflections were observed up to 30 mol% Eu^{3+} substitution in the Gd-based series, consistent with the very small ionic radius mismatch between Eu^{3+} ($r = 0.947$ Å, CN = 6) and Gd^{3+} ($r = 0.938$ Å, CN = 6). However, a slight shift of the diffraction peaks toward lower 2θ angles can be discerned for the La-based samples, which can be attributed to the larger ionic radius of La^{3+} ($r = 1.032$ Å, CN = 6) compared to Gd^{3+} , resulting in a modest lattice expansion. Considering the identical trivalent



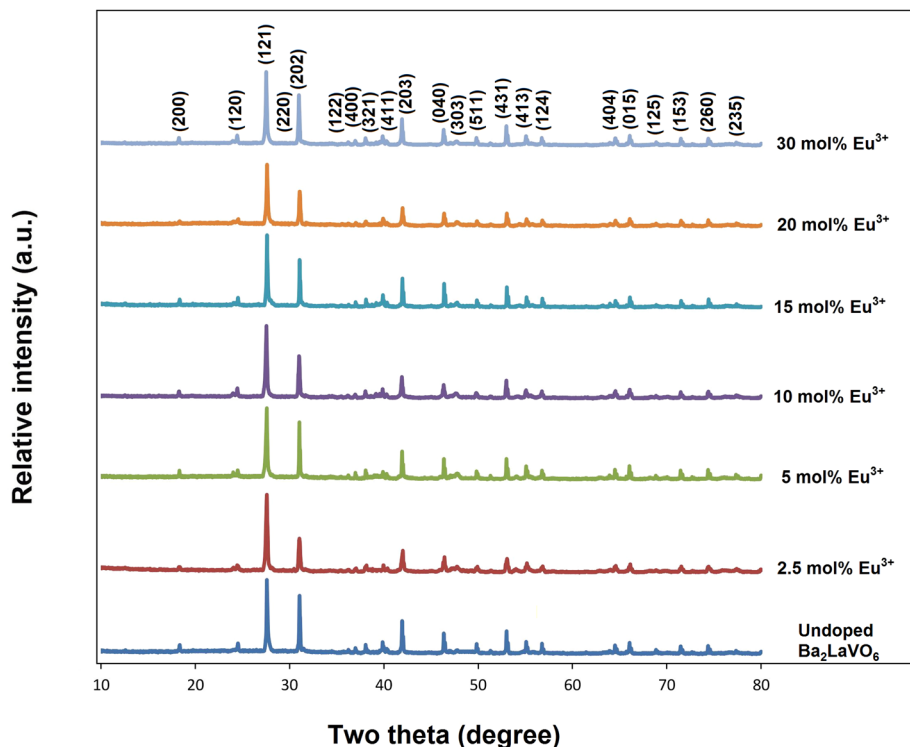


Fig. 1 X-ray diffraction (XRD) patterns of Ba₂La_{1-x}VO₆:xEu³⁺ phosphors with x = 0, 2.5, 5, 10, 15, 20, and 30 mol%, confirming single-phase orthorhombic perovskite formation.

charge state, Eu³⁺ ions are assumed to substitute La³⁺ or Gd³⁺ sites in the Ba₂LaVO₆ and Ba₂GdVO₆ lattices, respectively. This isoivalent substitution is further supported by the absence of

secondary phases and the small magnitude of the observed peak shifts, indicating a smooth incorporation of Eu³⁺ into the rare-earth sublattice rather than the V⁵⁺ site.

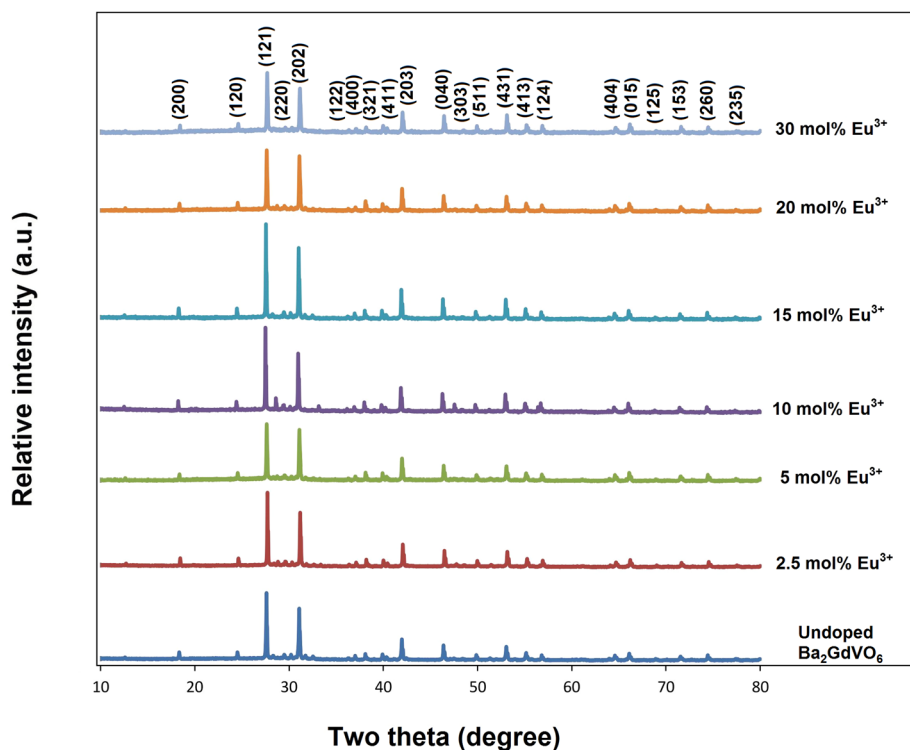


Fig. 2 X-ray diffraction (XRD) patterns of Ba₂Gd_{1-x}VO₆:xEu³⁺ phosphors with x = 0, 2.5, 5, 10, 15, 20, and 30 mol%, indexed to the orthorhombic Pnma structure.



To further validate the structural assignment, Rietveld refinements were carried out for representative compositions of Ba_2LaVO_6 and Ba_2GdVO_6 (Fig. 3a and b). The calculated profiles reproduce the experimental patterns with low residuals, confirming the suitability of the structural models and reaffirming the orthorhombic $Pnma$ symmetry for both hosts. As summarized in Table 1, Ba_2LaVO_6 refined to lattice parameters $a = 9.91 \text{ \AA}$, $b = 7.89 \text{ \AA}$, $c = 7.38 \text{ \AA}$, $V = 577.04 \text{ \AA}^3$ with residual factors $R_p = 6.14\%$, $R_{wp} = 8.13\%$, $\chi^2 \approx 2.21$, whereas Ba_2GdVO_6 refined to $a = 9.83 \text{ \AA}$, $b = 7.86 \text{ \AA}$, $c = 7.29 \text{ \AA}$, $V = 563.25 \text{ \AA}^3$ with $R_p = 4.33\%$, $R_{wp} = 5.56\%$, $\chi^2 \approx 1.66$. These values highlight the reliability of the refinements, as both R_p and R_{wp} remain below 10% with

acceptable χ^2 values close to 2. The comparison clearly shows that the La-based host exhibits a larger unit-cell volume ($\sim 2.45\%$ higher than Ba_2GdVO_6), which can be ascribed to the larger ionic radius of La^{3+} relative to Gd^{3+} . Moreover, the deviation among the a , b , and c parameters is slightly more pronounced in Ba_2LaVO_6 , reflecting a more anisotropic and distorted framework. In contrast, Ba_2GdVO_6 crystallizes in a more compact and rigid lattice, consistent with its smaller volume and more symmetric configuration. In summary, the combined XRD and Rietveld refinement analyses confirm that both $\text{Ba}_2\text{LaVO}_6:\text{Eu}^{3+}$ and $\text{Ba}_2\text{GdVO}_6:\text{Eu}^{3+}$ phosphors crystallize in a single phase orthorhombic $Pnma$ double perovskite

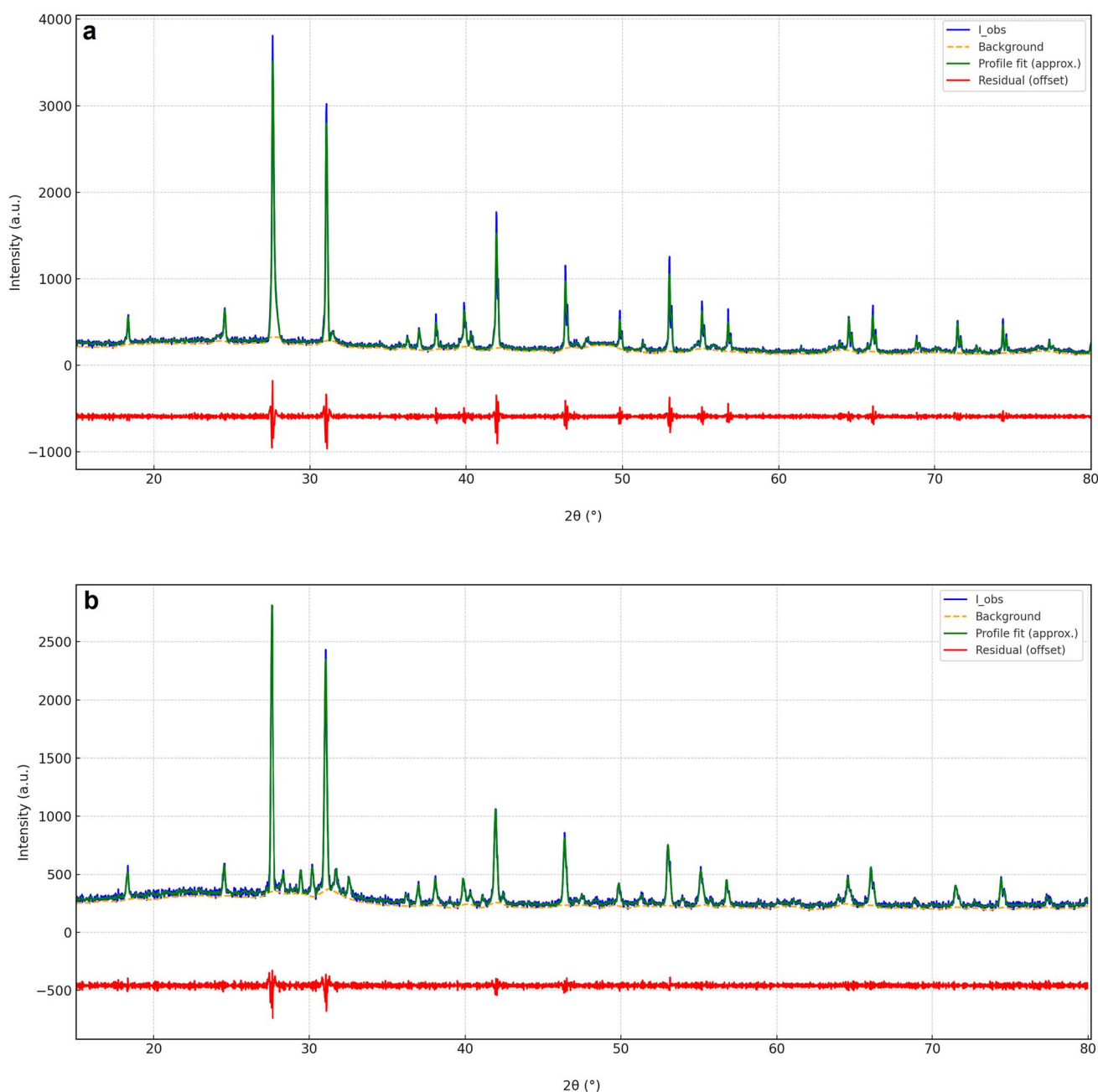


Fig. 3 Rietveld refinement profiles of the undoped double-perovskite hosts refined in the orthorhombic $Pnma$ space group: (a) Ba_2LaVO_6 and (b) Ba_2GdVO_6 . Observed, calculated, and difference patterns are shown.



Table 1 Rietveld refinement parameters of Ba₂LaVO₆ and Ba₂GdVO₆

Sample type	Rietveld refinement parameters	
Ba ₂ LaVO ₆	Symmetry	Orthorhombic
	Space group	<i>Pnma</i>
	<i>a</i> (Å)	9.91
	<i>b</i> (Å)	7.89
	<i>c</i> (Å)	7.38
	<i>V</i> (Å ³)	577.04
	<i>R_p</i>	6.14%
	<i>R_{wp}</i>	8.13%
Ba ₂ GdVO ₆	<i>χ</i> ²	2.21%
	Symmetry	Orthorhombic
	Space group	<i>Pnma</i>
	<i>a</i> (Å)	9.83
	<i>b</i> (Å)	7.86
	<i>c</i> (Å)	7.29
	<i>V</i> (Å ³)	563.25
	<i>R_p</i>	4.32%
<i>R_{wp}</i>	5.56%	
<i>χ</i> ²	1.66%	

structure, with successful incorporation of Eu³⁺ into the host lattices. The distinct differences in unit-cell volume, degree of orthorhombic distortion, and structural rigidity between the two hosts provide a robust structural basis for explaining their divergent photoluminescence behavior, particularly the contrasting dominance of the ⁵D₀ → ⁷F₂ and ⁵D₀ → ⁷F₄ transitions.

Fig. 4(a–d) and 5(a–d) present SEM micrographs of Ba₂-La_{1-x}VO₆:*x*Eu³⁺ and Ba₂Gd_{1-x}VO₆:*x*Eu³⁺ ceramics (*x* = 0, 5, 15, 30 mol%), respectively. In Fig. 4(a–d), the La-based series exhibits an aggregated and porous structure composed of

irregular morphologies arising from much finer subunits, with indistinct grain boundaries. In the examined Eu³⁺ doping range (0–30 mol%), La-based samples retain their clustered morphology, while no change in the uniform grain size trend is observed. In Fig. 5(a–d), the Gd-based series exhibits a markedly different microstructure, characterized by well-defined, faceted polyhedral grains with clear grain boundaries and a comparatively dense packing. The microstructure remains faceted with increasing Eu³⁺ content, and no significant change in grain size is observed, similar to the La-based structure. In summary, the SEM results indicate that the Gd-based host forms a more consolidated, grain-resolved ceramic microstructure, whereas the La-based host shows a more agglomerated and porous texture under the present synthesis conditions. These microstructural differences may contribute to variations in light scattering and emission extraction, while the dominant differences in emission pathway and concentration tolerance are primarily governed by the host-dependent local lattice environment discussed in the structural and optical sections.

X-ray photoelectron spectroscopy (XPS) was employed to verify the elemental composition and oxidation state of europium ions in the representative high-doping concentrations. Fig. 6a and c present the wide-scan (survey) XPS spectra for Ba₂La_{1-x}VO₆:0.3Eu³⁺ and Ba₂Gd_{1-x}VO₆:0.15Eu³⁺ samples, respectively. The survey spectra clearly confirm the presence of all constituent elements (Ba, La/Gd, V, O, and Eu) without detectable impurity-related signals, indicating successful incorporation of Eu into both host lattices. The high-resolution Eu 3d core-level spectra of Ba₂La_{1-x}VO₆:0.3Eu³⁺ and Ba₂Gd_{1-x}VO₆:0.15Eu³⁺ are shown in Fig. 6b and d, respectively. In both cases, the Eu 3d spectra exhibit characteristic doublet

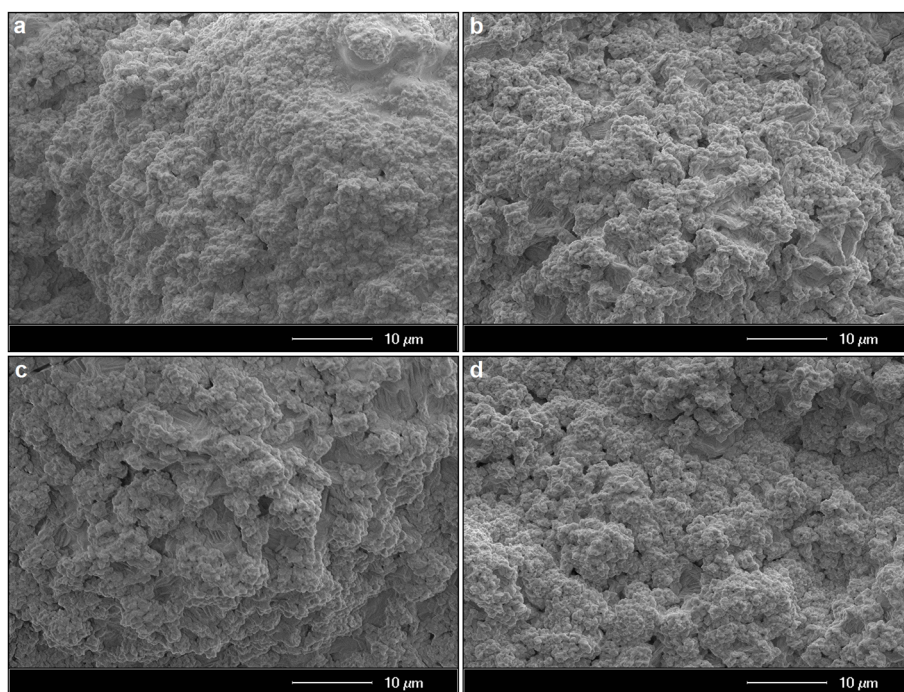


Fig. 4 SEM micrographs of La-based ceramic samples: (a) undoped Ba₂LaVO₆, (b) Ba₂La_{0.95}VO₆:0.05Eu³⁺, (c) Ba₂La_{0.85}VO₆:0.15Eu³⁺, and (d) Ba₂La_{0.70}VO₆:0.30Eu³⁺.



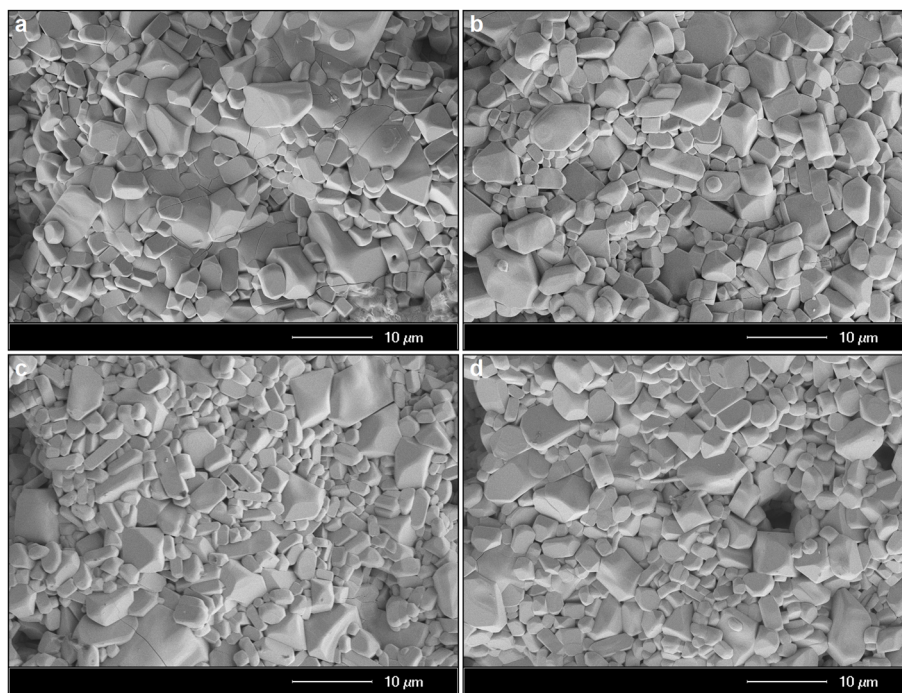


Fig. 5 SEM micrographs of Gd-based ceramic samples: (a) undoped Ba_2GdVO_6 , (b) $\text{Ba}_2\text{Gd}_{0.95}\text{VO}_6:0.05\text{Eu}^{3+}$, (c) $\text{Ba}_2\text{Gd}_{0.85}\text{VO}_6:0.15\text{Eu}^{3+}$, and (d) $\text{Ba}_2\text{Gd}_{0.70}\text{VO}_6:0.30\text{Eu}^{3+}$.

features corresponding to the $\text{Eu}^{3+} 3d_{5/2}$ and $\text{Eu}^{3+} 3d_{3/2}$ components, which are consistent with the trivalent Eu^{3+} oxidation state reported in the literature.^{11,12} Importantly, no additional components or phase features associated with Eu^{2+} ions are observed, confirming that Eu is stabilized exclusively in the trivalent state in both La-based and Gd-based hosts. The similarity of the Eu 3d binding energies in 30 mol% Eu^{3+} (Ba_2LaVO_6) and 15 mol% Eu^{3+} (Ba_2GdVO_6) further indicates that the local chemical environment of Eu^{3+} is comparable in both lattices, despite their different structural rigidity. Combined with the survey spectra, these results support the substitution of Eu^{3+} ions at the rare-earth ($\text{La}^{3+}/\text{Gd}^{3+}$) sites rather than at the Ba^{2+} or V^{5+} positions, in agreement with the isovalent charge state and compatible ionic radii. In addition, the quantitative elemental compositions derived from the XPS survey spectra are summarized in the corresponding tables for the La-based (Fig. 6a) and Gd-based (Fig. 6c) samples. The measured atomic percentages are in good agreement with the nominal stoichiometry within the experimental uncertainty of XPS analysis, supporting the reliable incorporation of Eu^{3+} into the host lattices. Overall, the XPS analysis provides direct evidence for the successful incorporation of Eu^{3+} into the double-perovskite framework without the formation of secondary Eu-containing phases, corroborating the structural and optical results discussed above.

3.2 Spectral properties and Judd–Ofelt parameters

Fig. 7a and c shows the excitation spectra of $\text{Ba}_2\text{LaVO}_6:\text{Eu}^{3+}$ (monitored at 696 nm, $^5\text{D}_0 \rightarrow ^7\text{F}_4$) and $\text{Ba}_2\text{GdVO}_6:\text{Eu}^{3+}$ (monitored at 611 nm, $^5\text{D}_0 \rightarrow ^7\text{F}_2$), respectively. The dominant

excitation band for $\text{Ba}_2\text{LaVO}_6:\text{Eu}^{3+}$ occurs at 395 nm, attributed to the $\text{Eu}^{3+} ^7\text{F}_0 \rightarrow ^5\text{L}_6$ transition, while weaker shoulders are observed in the 360–385 nm region, and an extremely weak $\text{O}^{2-} \rightarrow \text{Eu}^{3+}$ charge transfer band (CTB) between 250–320 nm. This pattern indicates that the population of the $^5\text{D}_0$ state proceeds mainly through direct 4f–4f excitation and selectively populates Eu^{3+} sites with a high branching into $^7\text{F}_4$, consistent with the abnormal-emission behavior observed in the PL spectra. In contrast, $\text{Ba}_2\text{GdVO}_6:\text{Eu}^{3+}$ displays its strongest excitation at 466 nm ($^7\text{F}_0 \rightarrow ^5\text{D}_2$), together with a well-resolved CTB in the UV range. The relative suppression of the 395 nm line and the presence of a strong CTB suggest more efficient host to Eu^{3+} energy transfer and a different local crystal field around Eu^{3+} in the Gd-based lattice compared with the La-based one. Consequently, these results indicate site-selective and host-dependent excitation processes: monitoring $^7\text{F}_4$ (696 nm) highlights near-ultraviolet $^7\text{F}_0 \rightarrow ^5\text{L}_6$ excitation in $\text{Ba}_2\text{LaVO}_6:\text{Eu}^{3+}$, while monitoring $^7\text{F}_2$ (611 nm) highlights blue $^7\text{F}_0 \rightarrow ^5\text{D}_2$ excitation in $\text{Ba}_2\text{GdVO}_6:\text{Eu}^{3+}$ with the aid of a stronger charge transfer band (CTB). Practically, $\text{Ba}_2\text{LaVO}_6:\text{Eu}^{3+}$ is most efficiently excited by near-UV light (~ 395 nm) and yields deep-red emission with a reinforced $^5\text{D}_0 \rightarrow ^7\text{F}_4$ component, while $\text{Ba}_2\text{GdVO}_6:\text{Eu}^{3+}$ is efficiently excited by blue light (~ 465 – 470 nm) and exhibits the conventional $^5\text{D}_0 \rightarrow ^7\text{F}_2$ -dominated orange-red emission.

Fig. 7b and d represent the photoluminescence (PL) spectra of $\text{Ba}_2\text{LaVO}_6:\text{Eu}^{3+}$ and $\text{Ba}_2\text{GdVO}_6:\text{Eu}^{3+}$, recorded under their most efficient excitation wavelengths at 395 nm and 466 nm, respectively. In both hosts, the characteristic Eu^{3+} emission transitions from the $^5\text{D}_0$ state are resolved at 591–594 nm ($^5\text{D}_0 \rightarrow ^7\text{F}_1$, magnetic-dipole), 615–611 nm ($^5\text{D}_0 \rightarrow ^7\text{F}_2$, electric-



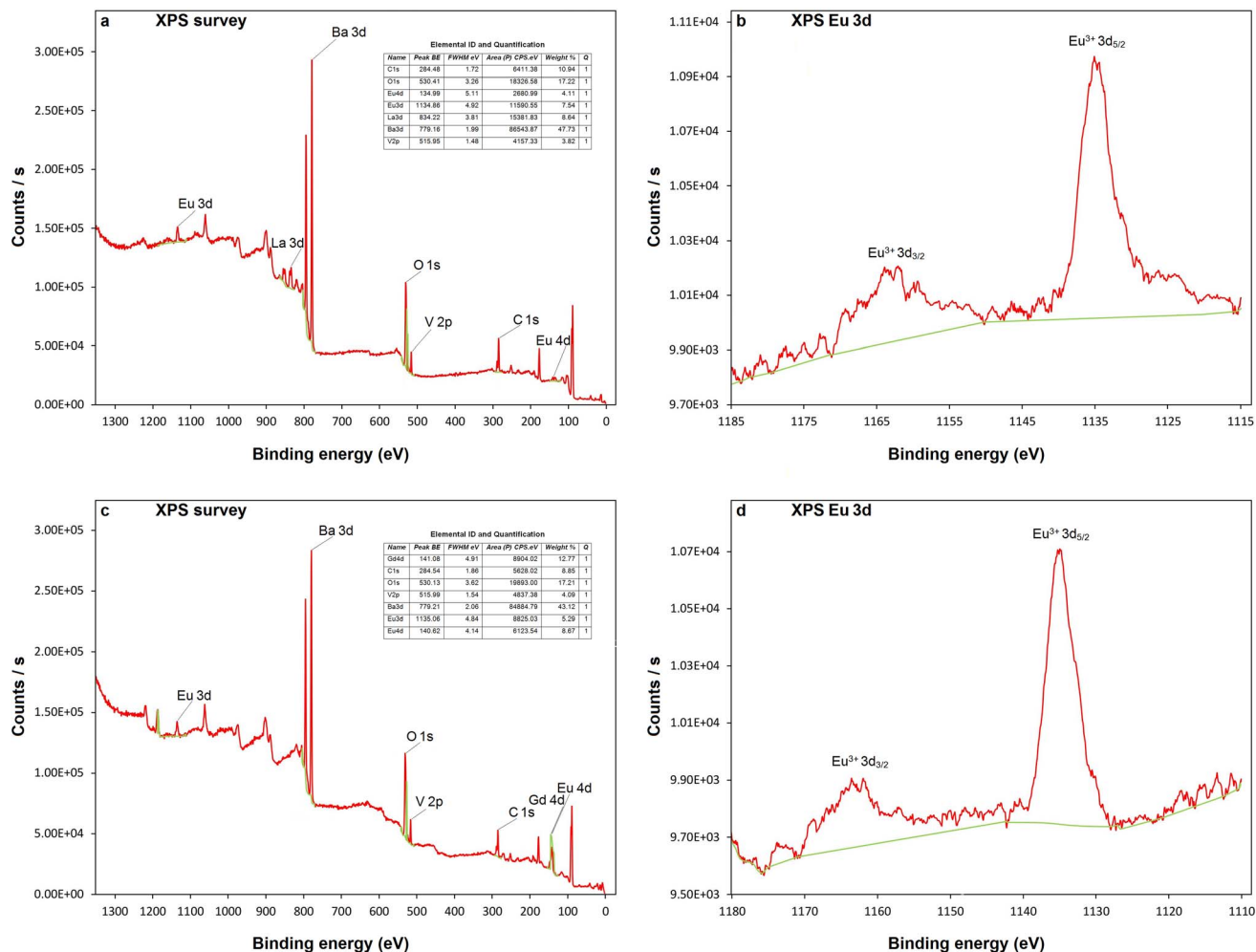


Fig. 6 X-ray photoelectron spectroscopy (XPS) analysis of representative high-doping samples: (a) survey spectrum and elemental composition of Ba₂Gd_{0.70}VO₆:0.30Eu³⁺, (b) high-resolution Eu 3d spectrum of Ba₂Gd_{0.70}VO₆:0.30Eu³⁺, (c) survey spectrum and elemental composition of Ba₂Gd_{0.85}VO₆:0.15Eu³⁺, and (d) high-resolution Eu 3d spectrum of Ba₂Gd_{0.85}VO₆:0.15Eu³⁺.

dipole), 651–654 nm (⁵D₀ → ⁷F₃), and 696–707 nm (⁵D₀ → ⁷F₄). The inset plots in Fig. 7b and d show that the integrated emission intensity of the La-based host increases monotonically with Eu³⁺ concentration up to 30 mol%, whereas the Gd-based host exhibits concentration quenching beyond 15 mol% Eu³⁺, respectively. For Ba₂LaVO₆:Eu³⁺, the ⁵D₀ → ⁷F₄ transition (696 nm) dominates the spectrum (Fig. 7b), exceeding the hypersensitive ⁵D₀ → ⁷F₂ transition—an unusual trend that corresponds to abnormal emission and agrees with the excitation-dependent intensity ratios where $I(\gamma_{F_4})/I(\gamma_{F_2}) > 1$ under 395 nm excitation. In contrast, Ba₂GdVO₆:Eu³⁺ excited at 466 nm (Fig. 7d) exhibits the conventional Eu³⁺ pattern with a dominant ⁵D₀ → ⁷F₂ emission and a weaker ⁵D₀ → ⁷F₄ transition. In this context, consistent with the PLE analysis, the CTB contribution is pronounced in Ba₂GdVO₆:Eu³⁺ but strongly suppressed in Ba₂LaVO₆:Eu³⁺, favoring direct f-f excitation in the latter. This behavior indicates that the La-based lattice can accommodate high Eu³⁺ contents, likely due to its greater structural flexibility and reduced probability of non-radiative cross-relaxation. In contrast, Ba₂GdVO₆:Eu³⁺ exhibits a clear

onset of concentration quenching beyond 15 mol%, reflecting enhanced non-radiative energy transfer between closely spaced Eu³⁺ ions in its more rigid and compact lattice framework. This interpretation is further supported by the systematic decrease in the asymmetry ratio $R_{F_2/F_1} = I(\gamma_{D_0 \rightarrow \gamma_{F_2}})/I(\gamma_{D_0 \rightarrow \gamma_{F_1}})$ with increasing Eu³⁺ concentration, which declines from 7.44 (2.5 mol%) to 2.74 (30 mol%). The reduction in R_{F_2/F_1} suggests a progressive decrease in local asymmetry around Eu³⁺ ions and a relative weakening of the hypersensitive ⁵D₀ → ⁷F₂ transition, consistent with increased ion-ion interactions and earlier concentration quenching. In summary, Ba₂LaVO₆:Eu³⁺ exhibits deeper-red emission with a reinforced ⁵D₀ → ⁷F₄ component and superior dopant tolerance within the investigated concentration range, whereas Ba₂GdVO₆:Eu³⁺ displays conventional orange-red emission dominated by the ⁵D₀ → ⁷F₂ transition but undergoes an earlier onset of concentration quenching. These findings highlight the strong structure-optical interplay in Eu³⁺-activated double perovskites, where lattice flexibility and local symmetry govern both emission characteristics and dopant tolerance.



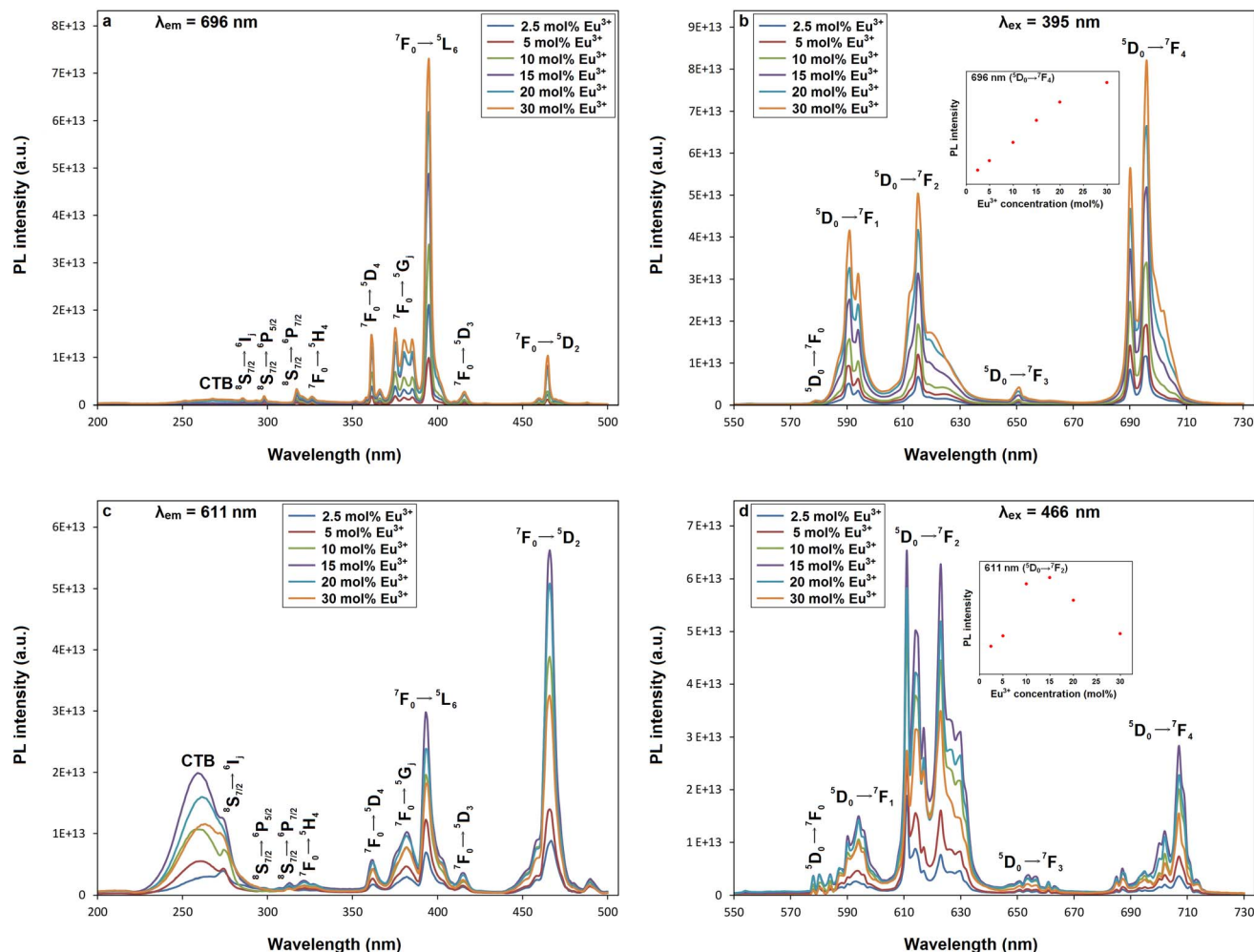


Fig. 7 PLE spectra of (a) $\text{Ba}_2\text{LaVO}_6:\text{Eu}^{3+}$ (monitored at 696 nm) and (c) $\text{Ba}_2\text{GdVO}_6:\text{Eu}^{3+}$ (monitored at 611 nm), and the corresponding PL emission spectra of (b) $\text{Ba}_2\text{LaVO}_6:\text{Eu}^{3+}$ under 395 nm excitation and (d) $\text{Ba}_2\text{GdVO}_6:\text{Eu}^{3+}$ under 466 nm excitation. Insets show the integrated emission intensity versus Eu^{3+} concentration; (b) 30 mol% for the La-based host and (d) concentration quenching beyond 15 mol% for the Gd-based host.

To quantitatively assess the anomalous emission behavior in $\text{Ba}_2\text{LaVO}_6:\text{Eu}^{3+}$, the PL spectra obtained under different excitation wavelengths are displayed in Fig. 8a, whereas Fig. 8b depicts the emission intensity ratio $R_{F_4/F_2} = I(^5\text{D}_0 \rightarrow ^7\text{F}_4) / I(^5\text{D}_0 \rightarrow ^7\text{F}_2)$ as a function of excitation wavelength. This ratio provides an effective indicator of excitation-dependent site selectivity related to the local coordination symmetry around Eu^{3+} ions; while the hypersensitive $^5\text{D}_0 \rightarrow ^7\text{F}_2$ transition is strongly enhanced in distorted and asymmetric environments, the $^5\text{D}_0 \rightarrow ^7\text{F}_4$ transition is generally less sensitive to local asymmetry and becomes relatively more pronounced when Eu^{3+} ions occupy more symmetric or rigid lattice sites. Upon excitation in the UV-near-UV region (263–395 nm), R_{F_4/F_2} increases monotonically from 0.80 (263 nm) to 1.55 (395 nm), corresponding to an overall ~ 1.9 -fold enhancement. This trend indicates that near-UV excitation—particularly the $^7\text{F}_0 \rightarrow ^5\text{L}_6$ transition at 395 nm—preferentially addresses Eu^{3+} sites that are inferred to possess higher local symmetry, thereby reinforcing the branching probability toward the $^7\text{F}_4$ manifold. This excitation-

dependent behavior is more clearly visualized in Fig. 8b, where the R_{F_4/F_2} ratio increases continuously from 263 to 395 nm and then decreases under blue excitation. As a result, $\text{Ba}_2\text{LaVO}_6:\text{Eu}^{3+}$ exhibits an abnormal emission pattern under 395 nm excitation, where the $^5\text{D}_0 \rightarrow ^7\text{F}_4$ emission (~ 700 nm) dominates over the hypersensitive $^5\text{D}_0 \rightarrow ^7\text{F}_2$ transition (~ 611 nm), yielding $R_{F_4/F_2} > 1$. Such dominance of the $^7\text{F}_4$ transition is uncommon for Eu^{3+} -activated phosphors and suggests that a significant fraction of Eu^{3+} ions reside in relatively symmetric and rigid coordination environments within the La-based lattice, which favor radiative decay into the $^7\text{F}_4$ level. In contrast, under blue-region excitation the R_{F_4/F_2} ratio decreases to 1.42 at 416 nm ($\approx ^7\text{F}_0 \rightarrow ^5\text{D}_3$) and further to 1.21 at 466 nm ($\approx ^7\text{F}_0 \rightarrow ^5\text{D}_2$). These excitation pathways populate a broader distribution of Eu^{3+} sites, including more distorted and lower-symmetry environments, thereby enhancing the electric-dipole-allowed $^5\text{D}_0 \rightarrow ^7\text{F}_2$ transition relative to $^5\text{D}_0 \rightarrow ^7\text{F}_4$. Consequently, the emission spectrum gradually reverts toward the conventional Eu^{3+} luminescence pattern dominated by the $^7\text{F}_2$ transition. The



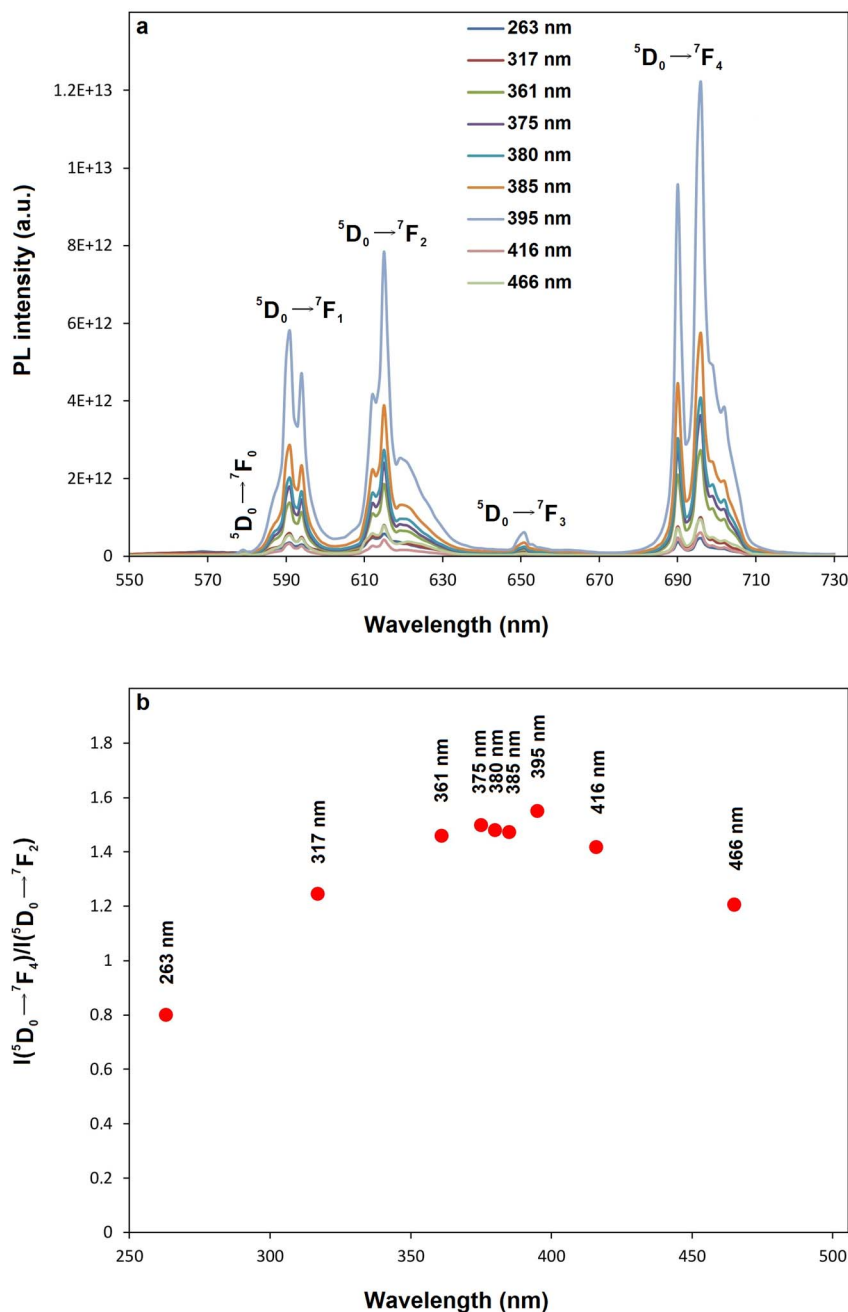


Fig. 8 (a) PL emission spectra of $\text{Ba}_2\text{LaVO}_6:\text{Eu}^{3+}$ phosphors recorded under different excitation wavelengths, (b) integrated emission intensity of the ${}^5D_0 \rightarrow {}^7F_4$ transition as a function of excitation wavelength.

excitation-dependent evolution of the R_{F_4/F_2} ratio clearly demonstrates that the anomalous ${}^5D_0 \rightarrow {}^7F_4$ dominance observed in $\text{Ba}_2\text{LaVO}_6:\text{Eu}^{3+}$ is not an intrinsic characteristic of Eu^{3+} emission but rather a site-selective phenomenon governed by excitation wavelength and the symmetry and rigidity of the La-based host lattice.

Judd–Ofelt theory provides a quantitative framework for analyzing the intensity of electron transitions within the 4f orbitals of rare-earth ions. It defines three key parameters, Q_J ($J = 2, 4, 6$), to characterize their spectral behavior.^{37,38} For Eu^{3+} , these parameters are extracted from the emission spectrum *via* eqn (1):^{39–46}

$$Q_J = \frac{S_{\text{MD}}(V_1^3)}{e^2(V_J^3)} \frac{9n^3}{n(n^2 + 2)^2} \frac{\int I_1(V_1)}{|\langle J \| U^J \| J' \rangle|^2 \int I_J(V_J)} \quad (1)$$

where I_1 and I_J are the integrated intensities of the ${}^5D_0 \rightarrow {}^7F_1$ and ${}^5D_0 \rightarrow {}^7F_J$ transitions respectively, V_1 and V_J their transition frequencies, $S_{\text{MD}} = 9.6 \times 10^{-42} \text{ esu}^2 \text{ cm}^2$ the magnetic dipole line strength, $e = 4.803 \times 10^{-10} \text{ esu}$ the elementary charge, n the refractive index, $|\langle J \| U^J \| J' \rangle|^2$ the double reduced matrix elements for unit tensor operators, J and J' are the total angular momentum of the initial and final states, respectively. Only the



electric dipole (ED) transitions ${}^5D_0 \rightarrow {}^7F_2$ ($U^2 = 0.0032$) and ${}^5D_0 \rightarrow {}^7F_4$ ($U^4 = 0.0023$), contribute nonzero matrix elements; the ${}^5D_0 \rightarrow {}^7F_6$ ($U^6 = 0.0002$) band is typically too weak in the PL spectrum and may be omitted with negligible impact on the overall Ω_J values.^{44–46} Finally, the spontaneous transition probability (A) is proportional to the corresponding dipole strength and can be expressed in terms of the Judd–Ofelt parameters, as given by eqn (2):^{39–46}

$$A(J, J') = \frac{64\pi^4 V^3}{3h(2J+1)} \left[\frac{n(n^2+2)^2}{9} \times S_{ED} + n^3 \times S_{MD} \right] \quad (2)$$

where h and n represent Planck's constant and the refractive index, respectively. The local field corrections χ_{ED} and χ_{MD} for the ED and MD transitions are $n(n^2+2)^2/9$ and n^3 , respectively. S_{ED} and S_{MD} are electric dipole and magnetic dipole line strengths ($\text{esu}^2 \text{cm}^2$). The electric dipole line strength (S_{ED}) related to JO parameters can be determined *via* eqn (3):

$$S_{ED}(J, J') = e^2 \sum_{J=2,4,6} \Omega_J \times |\langle J || U^J || J' \rangle|^2 \quad (3)$$

The refractive index (n) values can be estimated from the Lorenz–Lorentz formula eqn (4):^{44–46}

$$\frac{n^2 - 1}{n^2 + 2} \frac{1}{\rho} = \frac{\sum l_i r_i}{M} \quad (4)$$

where l_i refers to the atomic number of each element present in the compound's chemical formula, M stands for the molar mass, r_i denotes the specific refraction of the elements, and ρ presents the density of the compound, calculated using the formula $\rho = 1.661kM/\sum l_i r_i$, k is the cell packing coefficient. The refractive indexes for Ba_2LaVO_6 and Ba_2GdVO_6 were determined 2.306 and 2.277, respectively. The Judd–Ofelt intensity parameters (Ω_2 and Ω_4) for $\text{Ba}_2\text{LaVO}_6:\text{Eu}^{3+}$ and $\text{Ba}_2\text{GdVO}_6:\text{Eu}^{3+}$,

derived from the emission spectra, are summarized in Table 2. The Ω_2 parameter reflects the local asymmetry and covalency around Eu^{3+} ions, whereas Ω_4 is associated with the polarizability of the ligand field and the rigidity or flexibility of the host lattice.^{39–46} In the $\text{Ba}_2\text{LaVO}_6:\text{Eu}^{3+}$ series, Ω_2 shows a slight decrease from 1.824 to $1.651 \times 10^{-20} \text{cm}^2$ with increasing Eu^{3+} concentration, while Ω_4 decreases from 7.130 to $6.131 \times 10^{-20} \text{cm}^2$. The relatively low Ω_2 values indicate a comparatively symmetric and weakly covalent Eu^{3+} environment, whereas the persistently higher Ω_4 values signify a highly polarizable and dynamically flexible ligand field. This unusual $\Omega_4 > \Omega_2$ relationship directly correlates with the abnormal enhancement of the ${}^5D_0 \rightarrow {}^7F_4$ transition, accompanied by suppression of the hypersensitive ${}^5D_0 \rightarrow {}^7F_2$ channel. In contrast, $\text{Ba}_2\text{GdVO}_6:\text{Eu}^{3+}$ phosphor series exhibit significantly higher Ω_2 values at low Eu^{3+} concentrations (up to $10.080 \times 10^{-20} \text{cm}^2$), followed by a pronounced decrease to $3.602 \times 10^{-20} \text{cm}^2$ as the dopant content increases. This evolution indicates a progressive transition from a highly distorted local environment toward higher apparent centrosymmetry, consistent with the observed reduction of the asymmetry ratio $I({}^5D_0 \rightarrow {}^7F_2)/I({}^5D_0 \rightarrow {}^7F_1)$ from 7.44 to 2.74. Meanwhile, the Ω_4 values ($4.786\text{--}5.086 \times 10^{-20} \text{cm}^2$) remain lower than those of the La-based host, reflecting a more rigid and less polarizable lattice framework. As a result, the conventional ${}^5D_0 \rightarrow {}^7F_2$ electric-dipole transition dominates in $\text{Ba}_2\text{GdVO}_6:\text{Eu}^{3+}$. The pronounced decrease of Ω_2 with increasing Eu^{3+} concentration in the Gd-based host may be attributed to a combined effect of statistical site occupation and enhanced Eu–Eu interactions in the compact lattice, leading to effective crystal-field averaging. Under such conditions, Ω_2 should be regarded as an effective phenomenological parameter rather than a strictly site-specific descriptor, in agreement with the concurrent reductions in asymmetry ratio, decay lifetime, and quantum efficiency. Beyond this static interpretation, the

Table 2 Judd–Ofelt parameters (Ω_2 , Ω_4) and branching ratios (β) for $\text{Ba}_2\text{LaVO}_6:\text{Eu}^{3+}$ and $\text{Ba}_2\text{GdVO}_6:\text{Eu}^{3+}$ phosphor series

Eu ³⁺ conc. (x mol%)	Ba ₂ La _{1-x} VO ₆ :xEu ³⁺			Ba ₂ Gd _{1-x} VO ₆ :xEu ³⁺				
	Ω_2 (10 ⁻²⁰ cm ²)	Ω_4 (10 ⁻²⁰ cm ²)	Eu ³⁺ transitions	β (%)	Ω_2 (10 ⁻²⁰ cm ²)	Ω_4 (10 ⁻²⁰ cm ²)	Eu ³⁺ transitions	β (%)
2.5	1.824	7.130	${}^5D_0 \rightarrow {}^7F_1$	19.64	10.080	4.786	${}^5D_0 \rightarrow {}^7F_1$	9.42
			${}^5D_0 \rightarrow {}^7F_2$	27.35			${}^5D_0 \rightarrow {}^7F_2$	74.23
			${}^5D_0 \rightarrow {}^7F_4$	53.01			${}^5D_0 \rightarrow {}^7F_4$	16.35
5	1.777	6.447	${}^5D_0 \rightarrow {}^7F_1$	20.84	7.467	5.288	${}^5D_0 \rightarrow {}^7F_1$	11.42
			${}^5D_0 \rightarrow {}^7F_2$	28.29			${}^5D_0 \rightarrow {}^7F_2$	66.67
			${}^5D_0 \rightarrow {}^7F_4$	50.87			${}^5D_0 \rightarrow {}^7F_4$	21.91
10	1.666	6.730	${}^5D_0 \rightarrow {}^7F_1$	20.75	6.207	6.240	${}^5D_0 \rightarrow {}^7F_1$	12.32
			${}^5D_0 \rightarrow {}^7F_2$	26.39			${}^5D_0 \rightarrow {}^7F_2$	59.79
			${}^5D_0 \rightarrow {}^7F_4$	52.86			${}^5D_0 \rightarrow {}^7F_4$	27.89
15	1.699	6.405	${}^5D_0 \rightarrow {}^7F_1$	21.17	5.739	6.208	${}^5D_0 \rightarrow {}^7F_1$	12.92
			${}^5D_0 \rightarrow {}^7F_2$	27.47			${}^5D_0 \rightarrow {}^7F_2$	57.98
			${}^5D_0 \rightarrow {}^7F_4$	51.36			${}^5D_0 \rightarrow {}^7F_4$	29.10
20	1.738	6.315	${}^5D_0 \rightarrow {}^7F_1$	21.20	5.385	5.242	${}^5D_0 \rightarrow {}^7F_1$	14.07
			${}^5D_0 \rightarrow {}^7F_2$	28.12			${}^5D_0 \rightarrow {}^7F_2$	59.20
			${}^5D_0 \rightarrow {}^7F_4$	50.68			${}^5D_0 \rightarrow {}^7F_4$	26.73
30	1.651	6.131	${}^5D_0 \rightarrow {}^7F_1$	21.83	3.602	5.086	${}^5D_0 \rightarrow {}^7F_1$	17.67
			${}^5D_0 \rightarrow {}^7F_2$	27.50			${}^5D_0 \rightarrow {}^7F_2$	49.74
			${}^5D_0 \rightarrow {}^7F_4$	50.67			${}^5D_0 \rightarrow {}^7F_4$	32.59



results point to an excitation-selective and site-dependent emission mechanism. In Ba₂LaVO₆:Eu³⁺, near-UV excitation (⁷F₀ → ⁵L₆) efficiently populates the ⁵D₀ level within a polarizable lattice, selectively stabilizing radiative decay toward the ⁷F₄ manifold and giving rise to the observed abnormal emission. In contrast, the increasingly rigid and centrosymmetric environment in Ba₂GdVO₆:Eu³⁺ energetically favors the electric-dipole-allowed ⁵D₀ → ⁷F₂ transition while simultaneously enhancing non-radiative Eu–Eu energy transfer at higher dopant levels.

To contextualize these findings, Table 3 compares the Ω_2 and Ω_4 parameters obtained in this study with representative Eu³⁺-doped hosts reported in the literature.^{47–60} Notably, Ba₂La_{0.70}VO₆:0.30Eu³⁺ ($\Omega_2 = 1.651$, $\Omega_4 = 6.131 \times 10^{-20}$ cm²) falls into the class of systems where $\Omega_4 > \Omega_2$. Similar behavior has been documented for other compounds such as CoNb₂O₆:Eu³⁺, Li₂Zr(PO₄)₂:Eu³⁺, LiZnPO₄:Eu³⁺, and LiCdPO₄:Eu³⁺.^{47–54} The occurrence of $\Omega_4 > \Omega_2$ is relatively uncommon for Eu³⁺ systems, and its manifestation in Ba₂LaVO₆:Eu³⁺ is particularly relevant because it directly accounts for the abnormal dominance of the ⁵D₀ → ⁷F₄ transition. In contrast, Ba₂GdVO₆:Eu³⁺ (15 mol%) follows the more conventional $\Omega_2 > \Omega_4$ regime ($\Omega_2 = 5.739$, $\Omega_4 = 6.208 \times 10^{-20}$ cm²), consistent with strong local asymmetry and the dominance of the hypersensitive ⁵D₀ → ⁷F₂ transition. This trend aligns well with numerous reported Eu³⁺-doped systems such as Ca₂GdVO₆:Eu³⁺, Sr₂GdVO₆:Eu³⁺, Sr₂SiO₄:Eu³⁺, Sr₂MgSi₂O₇:Eu³⁺, and BaWO₄:Eu³⁺,^{55–60} where high Ω_2 values correlate with conventional red emission behavior. Thus, the Ω_4 -dominated La-based host favors anomalous ⁵D₀ → ⁷F₄ emission *via* lattice polarizability, while the Ω_2 -dominated Gd-based host exhibits conventional crystal-field-controlled emission.

The branching ratio (β) is an important optical parameter that provides insight into the radiative efficiency of Eu³⁺-doped phosphors and can be determined from the radiative transition probability (A_r or $A(J, J')$) and the total radiative transition probability ($\Sigma A(J, J')$) using eqn (5):

$$\beta(\%) = \frac{A(J, J')}{\sum A(J, J')} \times 100\% \quad (5)$$

In summary, the branching ratio (β) analysis provides clear evidence of the strong host-lattice dependence of the optical behavior in Ba₂LaVO₆:Eu³⁺ and Ba₂GdVO₆:Eu³⁺ phosphors. In Ba₂LaVO₆:Eu³⁺, relatively low β values (~26–28%) suppress the ⁵D₀ → ⁷F₂ transition but still sustain red luminescence, accompanied by an unusual reinforcement of the ⁵D₀ → ⁷F₄ transition. In contrast, Ba₂GdVO₆:Eu³⁺ exhibits significantly higher β values (49.74–74.23%), ensuring efficient electric-dipole transitions and highlighting its potential as a promising candidate for solid-state laser applications ($\beta \geq 50$).^{44–46} When considered together with the monotonic decrease in Ω_2 and the concurrent reduction in the spectral asymmetry ratio, these results indicate that Eu³⁺ ions in the Gd-based host undergo a doping-induced evolution toward increasingly symmetric local environments. This evolution stabilizes the conventional ⁵D₀ → ⁷F₂ emission mechanism while simultaneously accelerating concentration quenching through enhanced Eu–Eu interactions. In contrast, the La-based host maintains higher lattice polarizability and dynamic flexibility, thereby promoting the unusual enhancement of the ⁵D₀ → ⁷F₄ transition and yielding distinct luminescence fingerprints.

The decay profiles for Ba₂LaVO₆:Eu³⁺ and Ba₂GdVO₆:Eu³⁺ phosphor series with excitation 395, 466 nm and emission at 696, 611 nm, are illustrated in Fig. 9a and b, respectively. The decay profiles of the phosphors can be fitted to a mono-exponential or double-exponential model as described by eqn (6):⁶¹

$$I_t = I_0 + \sum_{i=1}^n I_i \times \exp\left(-\frac{t}{\tau_i}\right) \quad (6)$$

where, I_t is the PL intensity at time t after excitation, I_0 is the background intensity, and I_i , τ_i denote the amplitude and lifetime of the i -th decay component. For mono-exponential and double-

Table 3 Comparison of Judd–Ofelt intensity parameters (Ω_2 , Ω_4) for Eu³⁺-doped phosphors, highlighting Ω_4 -dominated and Ω_2 -dominated emission regimes

Phosphor	Eu ³⁺ concentration (%)	Ω_2 (10 ^{−20} cm ²)	Ω_4 (10 ^{−20} cm ²)	Ref.
Ba ₂ LaVO ₆ :Eu ³⁺	30	1.651	6.131	This study
Ba ₂ GdVO ₆ :Eu ³⁺	15	5.739	6.208	This study
Ca ₂ La ₃ (SiO ₄) ₃ F:Eu ³⁺	1	0.621	1.190	47
PbNb ₂ O ₆ :Eu ³⁺	6	2.251	2.604	48
Ca ₃ NbGa ₃ Si ₂ O ₁₄ :Eu ³⁺	5	1.277	2.208	49
KCaBi(PO ₄) ₂ :Eu ³⁺	21	1.773	2.043	50
K ₂ Zr(PO ₄) ₂ :Eu ³⁺	2	1.520	1.760	51
TiO ₂ :Eu ³⁺	5	0.210	0.560	52
Li ₂ Zr(PO ₄) ₂ :Eu ³⁺	2	0.230	2.140	53
BaTa ₂ O ₆ :Eu ³⁺ , B ³⁺	10	1.506	1.541	54
Ca ₂ GdVO ₆ :Eu ³⁺	15	10.263	2.385	55
Sr ₂ GdVO ₆ :Eu ³⁺	15	4.799	2.422	55
Sr ₂ SiO ₄ :Eu ³⁺	9	5.620	2.750	56
Sr ₂ MgSi ₂ O ₇ :Eu ³⁺	5	4.240	1.040	57
Na ₂ ZrO ₃ :Eu ³⁺	2	5.117	1.593	58
KZr ₂ (PO ₄) ₃ :Eu ³⁺	2	4.650	1.044	59
BaWO ₄ :Eu ³⁺	16	3.140	1.710	60



exponential decay models are $n = 1$ and $n = 2$, respectively. In this case, τ_1 and τ_2 represent the long and short lifetime components, respectively, with I_1 and I_2 being their associated intensities. To provide a quantitative comparison, the observed or average lifetime τ_{avg} or τ can be found using eqn (7):⁶¹

$$\tau = \frac{I_1\tau_1^2 + I_2\tau_2^2}{I_1\tau_1 + I_2\tau_2} \quad (7)$$

The corresponding average lifetimes (τ) are tabulated in Table 4. For the $\text{Ba}_2\text{LaVO}_6:\text{Eu}^{3+}$ system, the lifetime values show

only a minor decrease from 270 μs at 2.5 mol% to 233 μs at 30 mol%, resulting in closely overlapping decay profiles. This nearly stable decay behavior indicates that non-radiative cross-relaxation among Eu^{3+} ions remains limited even at high dopant concentrations, consistent with the PL results, which show the absence of severe concentration quenching up to 30 mol% and the sustained dominance of the $^5\text{D}_0 \rightarrow ^7\text{F}_4$ transition (Fig. 7b). By contrast, $\text{Ba}_2\text{GdVO}_6:\text{Eu}^{3+}$ exhibits a markedly different decay behavior. At low Eu^{3+} concentrations (2.5–5 mol%), the τ values are exceptionally long (627–652 μs), reflecting efficient radiative relaxation. However, with

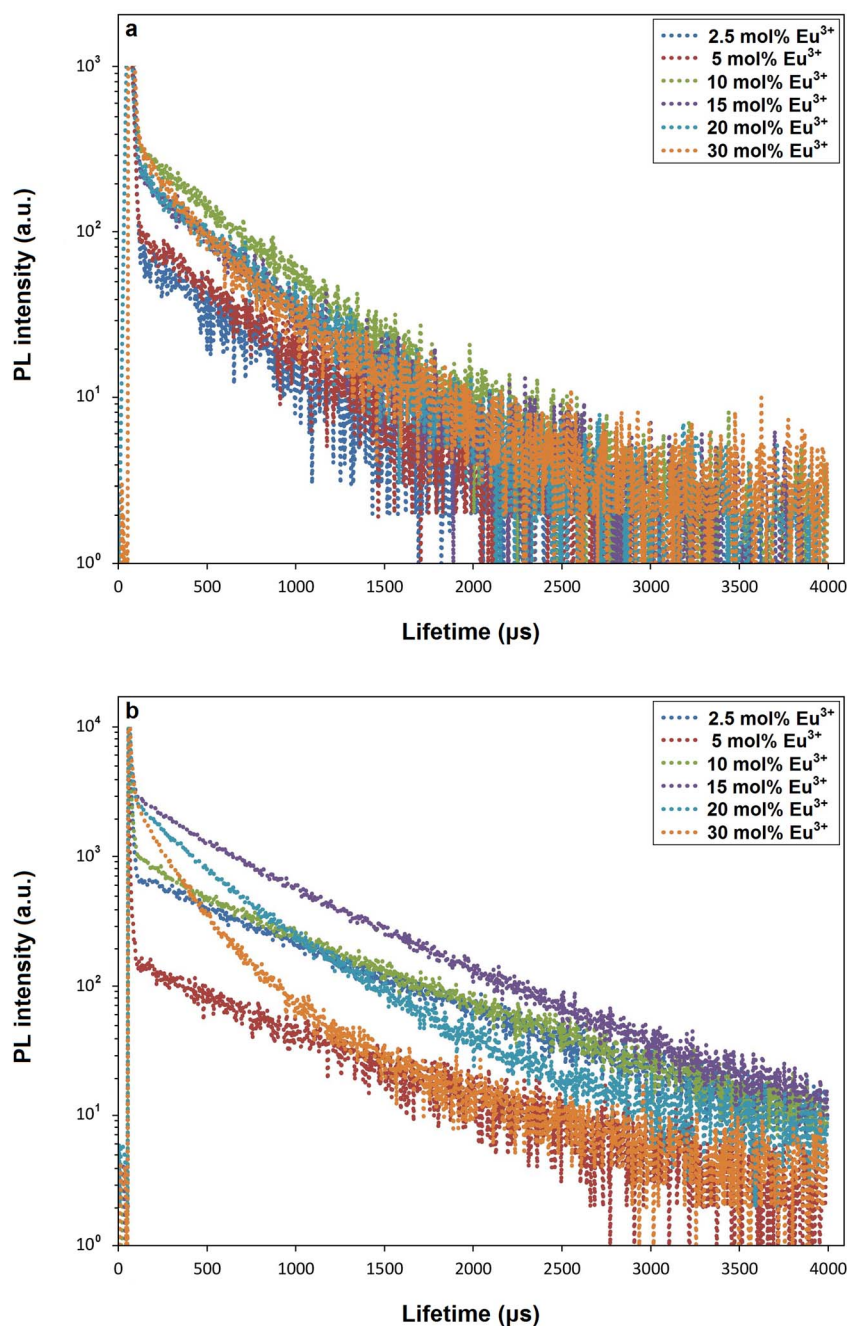


Fig. 9 Luminescence decay curves of (a) $\text{Ba}_2\text{LaVO}_6:\text{Eu}^{3+}$ and (b) $\text{Ba}_2\text{GdVO}_6:\text{Eu}^{3+}$ phosphors, excited at 395 and 466 nm and monitored at 696 nm ($^5\text{D}_0 \rightarrow ^7\text{F}_4$) and 611 nm ($^5\text{D}_0 \rightarrow ^7\text{F}_2$), respectively.



Table 4 Calculated radiative lifetimes (τ_r), observed lifetimes (τ), and calculated radiative quantum efficiencies (η_{QE} for $Ba_2MVO_6:Eu^{3+}$ (M = La, Gd) phosphor series

Eu ³⁺ conc. (x mol%)	Ba ₂ La _{1-x} VO ₆ :xEu ³⁺			Ba ₂ Gd _{1-x} VO ₆ :xEu ³⁺		
	τ_r (μ s)	τ (μ s)	η_{QE} (%)	τ_r (μ s)	τ (μ s)	η_{QE} (%)
2.5	1099	270	24.53	556	627	100<
5	1166	263	22.56	674	652	96.67
10	1161	256	22.02	727	614	84.39
15	1185	247	20.81	763	557	73.08
20	1186	247	20.80	830	362	43.66
30	1221	233	19.08	1042	196	18.77

increasing Eu³⁺ content, the lifetimes progressively shorten, reaching 196 μ s at 30 mol%. This pronounced lifetime reduction correlates well with the PL spectra (Fig. 7d), where concentration quenching becomes evident beyond 15 mol% Eu³⁺. Importantly, this decay trend is also consistent with the Judd–Ofelt (J–O) analysis and the evolution of the spectral asymmetry ratio. Both the Ω_2 parameter and the $I(^5D_0 \rightarrow ^7F_2)/I(^5D_0 \rightarrow ^7F_1)$ ratio decrease significantly with increasing Eu³⁺ concentration, indicating a gradual shift toward more symmetric and less covalent local environments around Eu³⁺ ions. Such a structural evolution weakens hypersensitive electric-dipole transitions and facilitates Eu–Eu multipolar interactions, thereby enhancing non-radiative energy transfer and cross-relaxation processes. In this context, the decay dynamics are fully consistent with the steady-state emission behavior: Ba₂LaVO₆:Eu³⁺ exhibits relatively stable lifetimes and a high tolerance to Eu³⁺ doping, supporting persistent abnormal ⁵D₀ → ⁷F₄-dominated emission, whereas Ba₂GdVO₆:Eu³⁺ shows initially long-lived emission followed by a rapid lifetime shortening at higher dopant levels, accounting for the earlier onset of concentration quenching and the conventional ⁵D₀ → ⁷F₂-dominated emission pattern. Thus, the decay analysis not only confirms the host-dependent quenching mechanisms but also provides dynamic evidence for distinct emission branching pathways in La-based and Gd-based double-perovskite hosts.

The radiative quantum efficiency (η_{QE}) calculated within the Judd–Ofelt (J–O) framework provides a theoretical estimate of the radiative contribution to the de-excitation of Eu³⁺ ions following optical excitation. According to eqn (8):

$$\eta_{QE} = \frac{A_r}{A_r + A_{nr}} = \frac{\tau}{\tau_r} \quad (8)$$

where A_r and A_{nr} are the radiative and non-radiative decay rates, respectively, τ_r is the radiative lifetime calculated from J–O analysis, and τ is the experimentally observed lifetime. As summarized in Table 4, the Ba₂LaVO₆:Eu³⁺ series exhibits calculated radiative lifetimes (τ_r) in the range of ~1099–1221 μ s, whereas the observed lifetimes (τ) vary between 270 and 233 μ s. This results in relatively low calculated radiative quantum efficiencies (~19–25%). The systematic decrease in η_{QE} with increasing Eu³⁺ concentration (from 24.5% at 2.5 mol% to 19.1% at 30 mol%) indicates enhanced non-radiative energy transfer among Eu³⁺ ions at higher dopant levels. This trend is consistent with the photoluminescence (PL) and decay results,

where the Ba₂LaVO₆:Eu³⁺ host accommodates high Eu³⁺ concentrations without abrupt quenching, yet exhibits a gradual reduction in radiative efficiency due to cross-relaxation and defect-assisted non-radiative processes. Importantly, the relatively low Ω_2 values obtained from J–O analysis, together with the suppressed asymmetry ratio, confirm that Eu³⁺ ions in the La-based host predominantly occupy more symmetric local environments. Such environments favor stable emission dominated by the unusual ⁵D₀ → ⁷F₄ transition, albeit with modest calculated radiative efficiency.

In contrast, the Ba₂GdVO₆:Eu³⁺ series shows significantly shorter calculated radiative lifetimes ($\tau_r \approx 556$ –1042 μ s), while the observed lifetimes ($\tau \approx 627$ μ s at 2.5 mol% Eu³⁺) are initially comparable to or even exceed τ_r . Consequently, the calculated radiative quantum efficiency approaches unity at low Eu³⁺ concentrations ($\approx 100\%$ at 2.5 mol% and $\approx 97\%$ at 5 mol%), indicating highly efficient radiative relaxation in the Gd-based host. However, with increasing Eu³⁺ content, η_{QE} decreases sharply (84% at 10 mol%, 74% at 15 mol%, 44% at 20 mol%, and $\sim 19\%$ at 30 mol%), reflecting strong concentration quenching. This pronounced efficiency loss correlates with the marked decrease in Ω_2 and the spectral asymmetry ratio, demonstrating that Eu³⁺ ions progressively evolve toward more symmetric and rigid local environments at higher doping levels. Such structural evolution enhances Eu–Eu multipolar interactions and facilitates non-radiative energy migration, leading to a rapid decline in calculated radiative quantum efficiency. In summary, the calculated radiative quantum efficiency analysis highlights a clear host-dependent contrast: Ba₂LaVO₆:Eu³⁺ supports higher Eu³⁺ incorporation with moderate but relatively stable η_{QE} ($\sim 20\%$), whereas Ba₂GdVO₆:Eu³⁺ exhibits near-unity η_{QE} at low doping but undergoes rapid efficiency degradation at higher concentrations due to symmetry-driven concentration quenching. This dual behavior is fully consistent with the PL, Judd–Ofelt, and decay analyses, confirming that lattice rigidity and local crystal-field evolution critically govern the balance between radiative and non-radiative energy dissipation in these double perovskite phosphors.

3.3 Thermal stability of photoluminescence

Fig. 10(a–d) illustrates the temperature-dependent photoluminescence (PL) behavior of the Eu³⁺ emission for Ba₂LaVO₆:Eu³⁺ (30 mol%) and Ba₂GdVO₆:Eu³⁺ (15 mol%)



phosphors measured in the 300–550 K range. These specific compositions were selected because they correspond to the highest Eu^{3+} concentrations exhibiting maximum or near-maximum emission intensity before the onset of severe concentration quenching in each host lattice, thereby representing the optimal operating regime for thermal stability assessment. The normalized integrated intensities (I/I_{300}) were analyzed using the Arrhenius-type relation (eqn (9)):^{62–71}

$$I = \frac{I_0}{1 + C \times \exp\left(-\frac{E_a}{kT}\right)} \quad (9)$$

where C denotes the pre-exponential factor associated with the concentration of thermally activated non-radiative centers, E_a is the activation energy for thermal quenching, and k is the Boltzmann constant. For the $\text{Ba}_2\text{LaVO}_6:\text{Eu}^{3+}$ (30 mol%) phosphor—where the $^5\text{D}_0 \rightarrow ^7\text{F}_4$ transition dominates—the PL intensity decreases gradually with increasing temperature, retaining about 41% of its room-temperature value at 550 K (Fig. 10a). The characteristic temperatures were interpolated

from the normalized emission intensities indicated in the inset of Fig. 10a, yielding $T_{0.9} \approx 332$ K and $T_{0.5} \approx 516$ K. Arrhenius fitting (Fig. 10b) yields activation energy of $E_a \approx 0.177$ eV and a C parameter of ≈ 53 , indicating a moderate thermal barrier accompanied by a relatively high probability of non-radiative processes. The more pronounced intensity drop above ~ 430 – 470 K (Fig. 10a) may be attributed to enhanced phonon coupling within the La–O sublattice and migration-assisted quenching at high Eu^{3+} concentrations. Nevertheless, the La-based host maintains efficient emission up to this temperature range, retaining $\sim 72\%$ of its initial intensity at ~ 430 K and $\sim 62\%$ at 470 K, confirming that its flexible lattice supports radiative transitions over a wide temperature window. By comparison, the $\text{Ba}_2\text{GdVO}_6:\text{Eu}^{3+}$ (15 mol%) phosphor exhibits superior thermal robustness (Fig. 10c). Its integrated PL intensity decreases more slowly with temperature, retaining approximately 57% of the initial emission at 550 K. Based on the normalized intensity values shown in the inset of Fig. 10c, the interpolated $T_{0.9} \approx 364$ K, while no half-intensity point is reached below 550 K, reflecting improved thermal endurance.

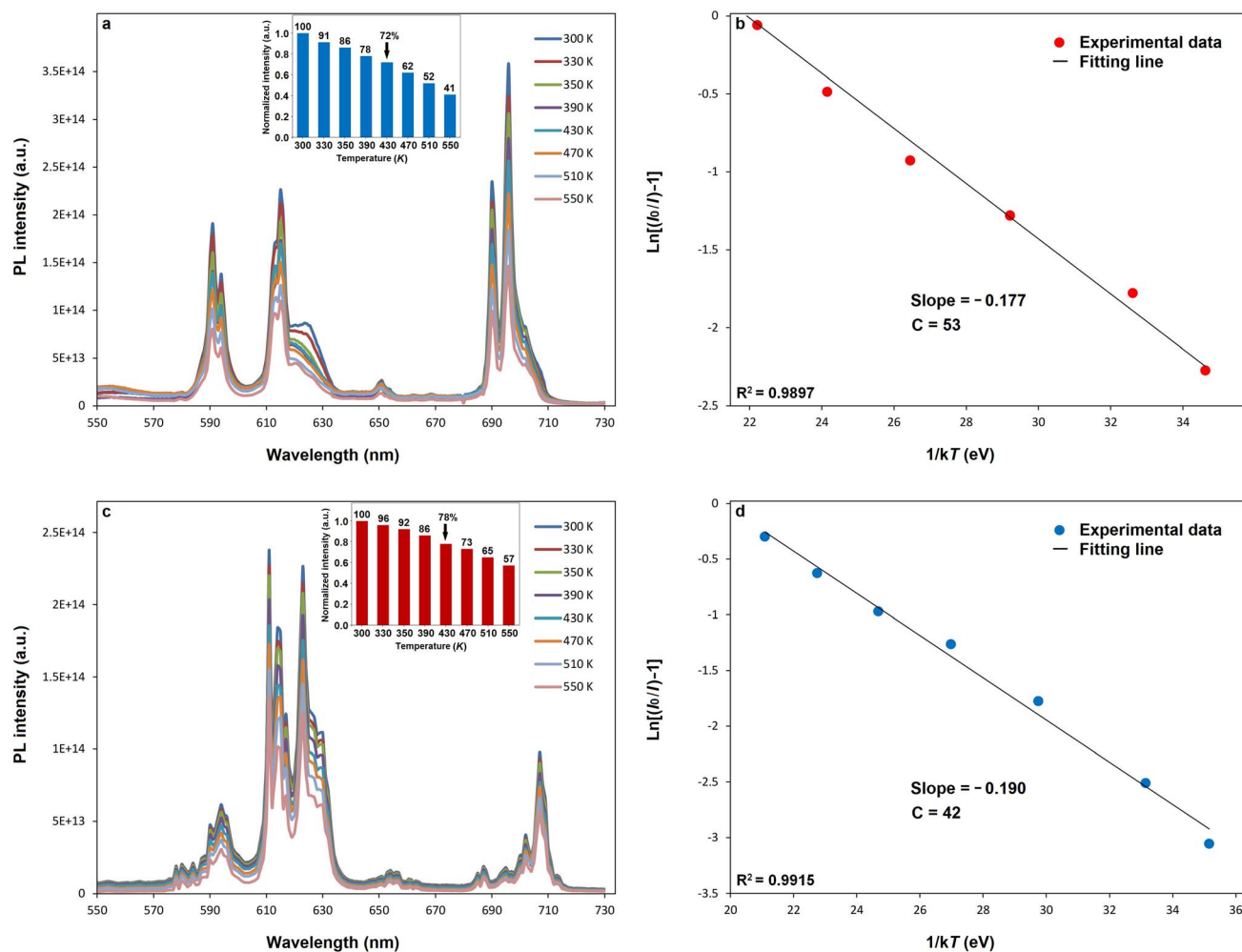


Fig. 10 Temperature-dependent photoluminescence behavior and Arrhenius analysis of PL intensity as a function of temperature between 300–550 K, (a) $\text{Ba}_2\text{LaVO}_6:\text{Eu}^{3+}$ (30 mol%, 696 nm) and (c) $\text{Ba}_2\text{GdVO}_6:\text{Eu}^{3+}$ (15 mol%, 611 nm) phosphors; (a), (c) the inset figures display the corresponding normalized intensity values (I/I_0) at selected temperatures, and (b), (d) Arrhenius plots of $\ln[(I/I_0)^{-1} - 1]$ versus $1/T$ used to extract the activation energy (E_a) and pre-exponential factor (C), respectively.



Arrhenius analysis (Fig. 10d) yields a slightly higher activation energy ($E_a \approx 0.190$ eV) and a lower C value (≈ 42), suggesting reduced involvement of thermally activated non-radiative centers compared with the La-based system. Consistently, the Gd-based phosphor retains $\sim 78\%$ of its room-temperature intensity at ~ 423 K (Fig. 10c), providing a comparable benchmark reference that highlights its gentler quenching slope and improved high-temperature endurance relative to the La-based system. This enhanced stability is attributed to the more compact lattice and stronger Gd–O bonding, which effectively suppresses multiphonon relaxation and defect-assisted quenching. Notably, the moderate activation energy combined with a larger C factor in $\text{Ba}_2\text{LaVO}_6:\text{Eu}^{3+}$ indicates that thermal quenching is governed not solely by barrier height but also by an increased probability of phonon-assisted non-radiative pathways. This interpretation is consistent with the Judd–Ofelt analysis, where higher Ω_4 values point to enhanced lattice polarizability and dynamic flexibility. Such an environment favors selective radiative relaxation into the ${}^7\text{F}_4$ level at room temperature, yet becomes increasingly susceptible to thermally activated multiphonon coupling at elevated temperatures.

Overall, $\text{Ba}_2\text{GdVO}_6:\text{Eu}^{3+}$ exhibits a slower quenching rate than $\text{Ba}_2\text{LaVO}_6:\text{Eu}^{3+}$, consistent with its higher E_a and smaller C parameter. Although both phosphors display comparable half-

intensity temperatures in the range of ~ 510 – 550 K, the Gd-based system shows a gentler high-temperature decay slope, confirming its superior thermal stability. These results demonstrate that the C parameter—reflecting the probability of defect-mediated non-radiative processes—is as critical as E_a in determining thermal quenching dynamics. The contrasting thermal behaviors correlate well with the structural and optical characteristics discussed in Sections 3.1–3.2. Rietveld refinement reveals that Ba_2LaVO_6 possesses a larger unit-cell volume (577.0 \AA^3) than Ba_2GdVO_6 (563.3 \AA^3), indicative of higher lattice polarizability and flexibility, which facilitate higher Eu^{3+} solubility but stronger phonon coupling. Conversely, the more compact Ba_2GdVO_6 lattice, characterized by stronger Gd–O bonding and reduced lattice relaxation, suppresses phonon-assisted quenching, yielding enhanced thermal stability ($I_{550}/I_{300} = 0.57$). Judd–Ofelt parameters further support this trend: higher Ω_4 values in $\text{Ba}_2\text{LaVO}_6:\text{Eu}^{3+}$ reflect a polarizable yet thermally sensitive environment, whereas lower Ω_4 in $\text{Ba}_2\text{GdVO}_6:\text{Eu}^{3+}$ signifies a rigid lattice that preserves the conventional ${}^5\text{D}_0 \rightarrow {}^7\text{F}_2$ -dominated emission. To place these thermal stability results in a broader context, Table 5 compares the activation energies and thermal quenching behavior of the present $\text{Ba}_2\text{LaVO}_6:\text{Eu}^{3+}$ and $\text{Ba}_2\text{GdVO}_6:\text{Eu}^{3+}$ phosphors with those of representative Eu^{3+} -activated red-emitting phosphors

Table 5 Comparison of thermal stability parameters (activation energy and intensity retention at 423 K) for Eu^{3+} -activated red-emitting phosphors

Phosphor	Eu^{3+} conc. (mol%)	λ_{ex} (nm)	E_a (eV)	I/I_0 (%) at 423 K	Reference
$\text{Ba}_2\text{LaVO}_6:\text{Eu}^{3+}$	30	397	~ 0.18	~ 72	This work
$\text{Ba}_2\text{GdVO}_6:\text{Eu}^{3+}$	15	397	~ 0.19	~ 78	This work
$\text{Na}_2\text{SrMg}(\text{PO}_4)_2:\text{Eu}^{3+}$	9	395	0.20	71	62
$\text{LiSrVO}_4:\text{Eu}^{3+}$	9	326	0.28	46	63
$\text{LiSrVO}_4:\text{Eu}^{3+}, 0.09\text{Na}^+$	9	326	0.29	69	63
$\text{Ba}_2\text{CaZn}_2\text{Si}_6\text{O}_{17}:\text{Eu}^{3+}$	9	395	0.17	69	64
$\text{Ca}_3\text{Al}_2\text{Ge}_3\text{O}_{12}:\text{Eu}^{3+}$	40	394	0.16	~ 79	65
$\text{Na}_3\text{Sc}_2(\text{PO}_4)_3:\text{Eu}^{3+}$	35	394	~ 0.23	~ 73	66
$\text{Y}_2(\text{MoO}_4)_3:\text{Eu}^{3+}$	7	395	0.31	~ 58	67
$\text{Ba}_3\text{Lu}_4\text{O}_9:\text{Eu}^{3+}$	25	396	0.21	64	68
$\text{Ca}_2\text{GdSbO}_6:\text{Eu}^{3+}$	50	464	~ 0.17	73	69
$\text{Sr}_2\text{LaTaO}_6:\text{Eu}^{3+}$	20	394	0.26	73	70
$\text{Ca}_2\text{GdNbO}_6:\text{Eu}^{3+}$	40	465	~ 0.17	~ 72	71
$\text{Ca}_2\text{GdTaO}_6:\text{Eu}^{3+}$	40	465	~ 0.17	~ 76	72

Table 6 CIE color coordinates, color purities and CCT parameters for $\text{Ba}_2\text{LaVO}_6:\text{Eu}^{3+}$ ($\lambda_{\text{ex}} = 396$ nm, $\lambda_{\text{em}} = 596$ nm), $\text{Ba}_2\text{GdVO}_6:\text{Eu}^{3+}$ ($\lambda_{\text{ex}} = 466$ nm, $\lambda_{\text{em}} = 611$ nm) phosphor series

Eu^{3+} con. (x mol%)	$\text{Ba}_2\text{La}_{1-x}\text{VO}_6:\text{xEu}^{3+}$				$\text{Ba}_2\text{Gd}_{1-x}\text{VO}_6:\text{xEu}^{3+}$			
	CIE coordinates		Color purity (%)	CCT (K)	CIE coordinates		Color purity (%)	CCT (K)
x	y	x			y			
2.5	0.6305	0.3690	76.34	1821	0.6670	0.3328	98.92	2971
5	0.6250	0.3746	75.22	1745	0.6579	0.3418	96.44	2562
10	0.6341	0.3655	77.10	1881	0.6628	0.3369	97.77	2773
15	0.6337	0.3659	77.01	1874	0.6679	0.3320	99.17	3012
20	0.6362	0.3634	77.54	1922	0.6548	0.3449	95.61	2443
30	0.6364	0.3632	77.58	1926	0.6343	0.3652	90.35	1886



reported in the literature.^{62–71} As summarized in Table 5, the present $\text{Ba}_2\text{LaVO}_6:\text{Eu}^{3+}$ and $\text{Ba}_2\text{GdVO}_6:\text{Eu}^{3+}$ phosphors exhibit activation energies of ~ 0.18 and ~ 0.19 eV, respectively, together with high emission retention at elevated temperature. Notably, the integrated intensity retained at 423 K reaches $\sim 72\%$ for $\text{Ba}_2\text{LaVO}_6:\text{Eu}^{3+}$ (30 mol%) and $\sim 78\%$ for $\text{Ba}_2\text{GdVO}_6:\text{Eu}^{3+}$ (15 mol%), values that are comparable to or exceed those reported for many oxide-based and phosphate-based Eu^{3+} phosphors, even though the present systems operate at relatively high Eu^{3+} concentrations. This comparison highlights that the balanced lattice rigidity and phonon coupling inherent to the double-perovskite framework enable competitive thermal

robustness while preserving high dopant tolerance, positioning these materials favorably among reported Eu^{3+} -activated red phosphors.

3.4 Colorimetric analysis

The colorimetric characteristics of $\text{Ba}_2\text{LaVO}_6:\text{Eu}^{3+}$ and $\text{Ba}_2\text{GdVO}_6:\text{Eu}^{3+}$ phosphors were analyzed using the CIE 1931 chromaticity diagram (Fig. 11a and b). The corresponding chromaticity coordinates (x, y), color purity (CP), and correlated color temperature (CCT) values are summarized in Table 6. These parameters provide quantitative insight into the emission hue, spectral saturation, and perceived warmth of the

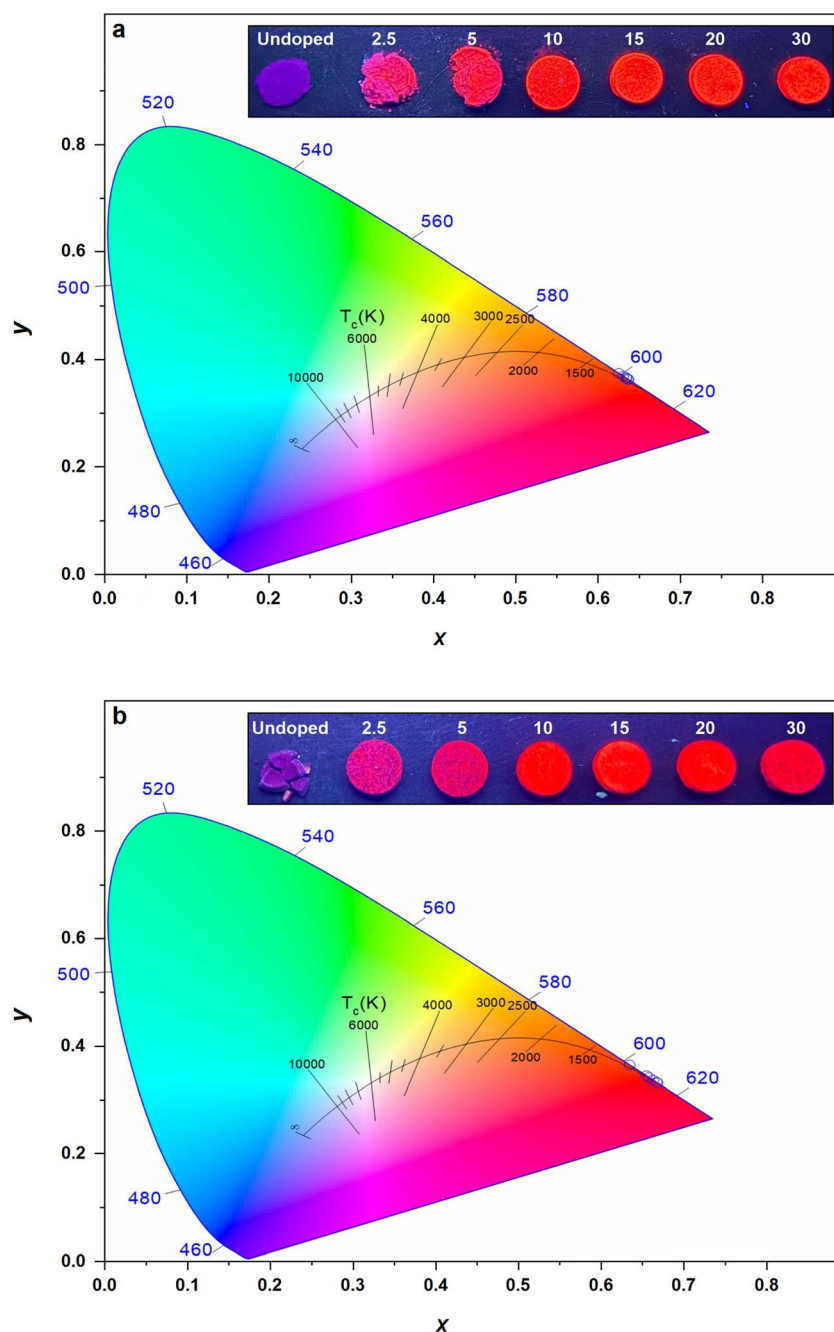


Fig. 11 CIE chromaticity diagrams and UV lamp photographs under 365 nm excitation for (a) $\text{Ba}_2\text{LaVO}_6:\text{Eu}^{3+}$ and (b) $\text{Ba}_2\text{GdVO}_6:\text{Eu}^{3+}$ phosphors.



emitted light—key factors for lighting and display applications. The color purity, which expresses the degree of spectral saturation relative to ideal monochromatic emission, was calculated using eqn (10):^{71–74}

$$\text{Color purity} = \frac{\sqrt{(x - x_i)^2 + (y - y_i)^2}}{\sqrt{(x_d - x_i)^2 + (y_d - y_i)^2}} \times 100 \quad (10)$$

where $(x_i, y_i) = (0.313, 0.329)$ are the coordinates of the standard white point, and (x_d, y_d) denote those of the dominant wavelength. The correlated color temperature (CCT), representing the perceptual warmth or coolness of the emission, was estimated using McCamy's empirical eqn (11):⁷⁵

$$\text{CCT} = -449n^3 + 3525n^2 - 6823n + 5520.33 \quad (11)$$

where $n = (x - x_i)/(y - y_i)$. The colorimetric analysis reveals distinct host-dependent behaviors (Fig. 11 and Table 6). For $\text{Ba}_2\text{LaVO}_6:\text{Eu}^{3+}$, the chromaticity coordinates ($x \approx 0.625\text{--}0.636$, $y \approx 0.363\text{--}0.375$) fall into the orange-red region, with color purity values around 75–78%. This is somewhat unexpected considering the abnormal reinforcement of the $^5\text{D}_0 \rightarrow ^7\text{F}_4$ transition in this host, which would suggest a deeper red output. The discrepancy arises because the 700 nm emission band lies in a region of low photopic eye sensitivity, thus contributing less to the CIE chromaticity than the stronger 611 nm $^5\text{D}_0 \rightarrow ^7\text{F}_2$ transition. As a result, despite the unusual spectral dominance of $^5\text{D}_0 \rightarrow ^7\text{F}_4$, the La-host series appears shifted toward orange-red in the CIE diagram. In contrast, $\text{Ba}_2\text{GdVO}_6:\text{Eu}^{3+}$ phosphors exhibit CIE coordinates that move further into the red region ($x \approx 0.634\text{--}0.668$, $y \approx 0.332\text{--}0.365$) with substantially higher color purity values (90–99%) across most doping levels. This behavior is consistent with the conventional dominance of the $^5\text{D}_0 \rightarrow ^7\text{F}_2$ transition, which falls in the eye's region of high sensitivity, thereby yielding more saturated red coordinates in the CIE diagram even though the $^5\text{D}_0 \rightarrow ^7\text{F}_4$ contribution is weaker. At higher Eu^{3+} concentrations, multipole–multipole interactions and concentration quenching broaden the emission, leading to a slight reduction in color purity (e.g., 90.35% at 30 mol% Eu^{3+}). The CCT values for both hosts remain below 3000 K, confirming their classification as warm-light phosphors. $\text{Ba}_2\text{LaVO}_6:\text{Eu}^{3+}$ exhibits lower CCT values (1745–1926 K), reflecting a warmer but less saturated orange-red emission. By contrast, $\text{Ba}_2\text{GdVO}_6:\text{Eu}^{3+}$ yields somewhat higher CCT values (1886–3012 K) due to the stronger $^5\text{D}_0 \rightarrow ^7\text{F}_2$ contribution, yet still remains within the warm-red category. Overall, these findings demonstrate that while $\text{Ba}_2\text{LaVO}_6:\text{Eu}^{3+}$ provides a unique example of spectral abnormality ($^5\text{D}_0 \rightarrow ^7\text{F}_4$ enhancement) that is not fully captured in CIE space, $\text{Ba}_2\text{GdVO}_6:\text{Eu}^{3+}$ delivers visually deeper red coordinates with higher color purity, underlining the complementary optical advantages of La-based and Gd-based double perovskite hosts. Furthermore, the photographs taken under 365 nm UV excitation (the insets of Fig. 11a and b) provide visual confirmation of the colorimetric analysis: $\text{Ba}_2\text{LaVO}_6:\text{Eu}^{3+}$ exhibits a bright orange-red glow, whereas $\text{Ba}_2\text{GdVO}_6:\text{Eu}^{3+}$ displays a deeper and more saturated red emission, consistent with the

chromaticity coordinates and color purity trends summarized in Table 6. The complementary optical behavior of these La-based and Gd-based double perovskites highlights how lattice rigidity and spectral selectivity co-shape their color performance under near-ultraviolet excitation.

4. Conclusion

This work presents a systematic comparison of $\text{Ba}_2\text{LaVO}_6:\text{Eu}^{3+}$ and $\text{Ba}_2\text{GdVO}_6:\text{Eu}^{3+}$ double perovskite phosphors, clarifying how host-lattice rigidity governs Eu^{3+} emission behavior, dopant tolerance, and thermal stability. X-ray diffraction and Rietveld refinement confirm that both systems crystallize in the orthorhombic $Pnma$ structure, while SEM reveals distinct host-dependent microstructural characteristics, consistent with the relatively flexible La-based lattice and the more rigid Gd-based framework. XPS analysis further verifies the exclusive presence of Eu^{3+} in representative high-doping compositions, confirming successful lattice incorporation without secondary phases. Owing to its larger unit-cell volume and higher lattice polarizability, $\text{Ba}_2\text{LaVO}_6:\text{Eu}^{3+}$ stabilizes an abnormal emission process dominated by the $^5\text{D}_0 \rightarrow ^7\text{F}_4$ transition under near-UV excitation, accompanied by high Eu^{3+} solubility up to 30 mol% without severe concentration quenching. This behavior is supported by $\Omega_4 > \Omega_2$ Judd–Ofelt parameters, excitation-dependent branching ratios, nearly invariant decay lifetimes, and moderate radiative quantum efficiency. Despite its unconventional emission behavior, the La-based phosphor retains ~41% of its room-temperature intensity at 550 K, indicating robust thermal stability. In contrast, $\text{Ba}_2\text{GdVO}_6:\text{Eu}^{3+}$ follows the conventional Eu^{3+} emission scheme dominated by the hypersensitive $^5\text{D}_0 \rightarrow ^7\text{F}_2$ transition. The rigid lattice enables high radiative efficiency and excellent color purity at low dopant concentrations, but enhanced Eu–Eu interactions lead to concentration quenching beyond ~15 mol%. The higher activation energy and lower pre-exponential factor derived from thermal quenching analysis indicate reduced phonon-assisted non-radiative losses and superior intrinsic lattice stability relative to the La-based host. CIE chromaticity analysis confirms that the La-based host yields a warm orange-red emission with moderate color purity despite abnormal $^5\text{D}_0 \rightarrow ^7\text{F}_4$ reinforcement, while the Gd-based host delivers visually deeper red emission with higher color purity owing to the conventional dominance of the $^5\text{D}_0 \rightarrow ^7\text{F}_2$ transition. Overall, this comparative study establishes host-lattice rigidity as a decisive parameter controlling emission branching, dopant tolerance, and thermal quenching in Eu^{3+} -activated Ba_2MVO_6 ($M = \text{La}, \text{Gd}$) phosphors. The La-based hosts favor structural flexibility and unconventional $^5\text{D}_0 \rightarrow ^7\text{F}_4$ reinforcement, whereas Gd-based hosts provide rigid-lattice stabilization, high radiative efficiency, and saturated red emission within a narrower doping window. These insights provide fundamental guidelines for host-controlled emission tuning in double perovskite phosphors, rather than focusing on direct device-oriented optimization.

Conflicts of interest

There are no conflicts to declare.



Data availability

The data that supports the current research can be made available upon reasonable request to the corresponding author.

References

- 1 B. R. R. Krushna, D. Kavyashree, S. P. Chakradhar, S. C. Sharma, R. J. Mohan, G. R. Revannasiddappa, S. Mishra, K. Manjunatha, S. Y. Wu, S. L. Yu, H. H. Chi, Sa. Sangaraju, M. Shkir and H. Nagabhushana, Red emitting Eu^{3+} doped $\text{Ba}_2\text{La}_4\text{Zn}_2\text{O}_{10}$ phosphors with high thermal stability for forensic and photoluminescent applications, *Inorg. Chem. Commun.*, 2026, **186**, 116144, DOI: [10.1016/j.inoche.2026.116144](https://doi.org/10.1016/j.inoche.2026.116144).
- 2 Y. Ren, Z. Xuan, J. Yang, J. Chang, Y. Jia, X. Yin, Y. Liu, J. A. Wang and G. Henkelman, Tunable optical properties and enhanced stability of organic-inorganic hybrid Cu-based halide thin films for advanced anti-counterfeiting applications, *Laser Photonics Rev.*, 2025, DOI: [10.1002/lpor.202501078](https://doi.org/10.1002/lpor.202501078).
- 3 P. Abhiraj, C. Vishal, P. Sahana, N. S. Reddy, R. T. Gowda, C. S. P. Kumar, S. Akshay, Tejas, G. S. Hegde, S. D. Kamath and B. P. Siddalingeshwara, Structural, optical, and Judd-Ofelt spectroscopic analysis of Dy^{3+} doped borate-based oxyfluoride glasses exhibiting enhanced UV excitable-yellow luminescence for advanced photonic applications, *J. Alloys Compd.*, 2026, **1050**, 185786, DOI: [10.1016/j.jallcom.2025.185786](https://doi.org/10.1016/j.jallcom.2025.185786).
- 4 M. İlhan, L. F. Güleriyüz, M. K. Ekmekçi and M. Erdem, Multicolor emission of $\text{CdNb}_2\text{O}_6:\text{Eu}^{3+}$, Er^{3+} and $\text{CdNb}_2\text{O}_6:\text{Eu}^{3+}$, Er^{3+} , Yb^{3+} phosphors with dual excitation and dual emission in UV to IR for latent fingerprint applications, *Opt. Mater.*, 2025, **166**, 117178, DOI: [10.1016/j.optmat.2025.117178](https://doi.org/10.1016/j.optmat.2025.117178).
- 5 S. Khondara, P. Yasaka, K. Boonin and J. Kaewkhao, Green Light Emission from Tb^{3+} ion doped boro-tellurite glass potential for scintillation and thermoluminescence material application, *Thai J. Nanosci. Nanotechnol.*, 2025, **10**, 51–66, DOI: [10.55003/tjnn10120255](https://doi.org/10.55003/tjnn10120255).
- 6 J. H. Han, J. M. Sim and Y. S. Lee, Multi-color photoluminescence and persistent luminescence of Eu^{3+} -doped Zn_2GeO_4 for security applications, *J. Alloys Compd.*, 2025, **1026**, 180457, DOI: [10.1016/j.jallcom.2025.180457](https://doi.org/10.1016/j.jallcom.2025.180457).
- 7 M. İlhan and İ. Ç. Keskin, Evaluation of the structural, near-infrared luminescence, and radioluminescence properties of Nd^{3+} activated TTB-lead metatantalate phosphors, *J. Turk. Chem. Soc., Sect. A*, 2023, **10**, 453–464, DOI: [10.18596/jotcsa.1216564](https://doi.org/10.18596/jotcsa.1216564).
- 8 R. Raina, M. L. Verma, N. Chakraborty, K. Pathania and P. Biswas, DFT and Judd-Ofelt analysis of a novel red-emitting Eu^{3+} doped KSrB_5O_9 phosphor for photonic applications, *J. Alloys Compd.*, 2026, **1050**, 185578, DOI: [10.1016/j.jallcom.2025.185578](https://doi.org/10.1016/j.jallcom.2025.185578).
- 9 V. Mishra, S. J. Sharma and H. Borkar, Enhanced photoluminescent properties of Eu^{3+} doped CaMoO_4 nanoparticles: Experimental and theoretical approach, *Phys. B*, 2026, **723**, 418141, DOI: [10.1016/j.physb.2025.418141](https://doi.org/10.1016/j.physb.2025.418141).
- 10 A. A. Saleh, H. Z. Hamamera, H. K. Khanfar, A. F. Qasrawi and G. Yumusak, Gd and Tb doping effects on the physical properties of $\text{Nd}_2\text{Sn}_2\text{O}_7$, *Mater. Sci. Semicond. Process.*, 2018, **88**, 256–261, DOI: [10.1016/j.mssp.2018.08.017](https://doi.org/10.1016/j.mssp.2018.08.017).
- 11 W. Q. Liu, D. Wu, H. Chang, R. X. Duan, W. J. Wu, G. Amu, K. F. Chao, F. Q. Bao and O. Tegus, The enhanced red emission and improved thermal stability of $\text{CaAlSiN}_3:\text{Eu}^{2+}$ phosphors by using nano- EuB_6 as raw material, *Nanomater*, 2018, **8**, 66, DOI: [10.3390/nano8020066](https://doi.org/10.3390/nano8020066).
- 12 J. Shu, Z. Jia, E. Damiano, H. Wang, Y. Yin, N. Lin, X. Zhao, X. Xu, M. Tonelli and X. Tao, Charge compensations of Eu^{2+} and O_i^{2-} co-exist in $\text{Eu}^{3+}:\text{CaMoO}_4$ single-crystal fibers grown by the micro-pulling-down method, *CrystEngComm*, 2018, **20**, 6741–6751, DOI: [10.1039/C8CE01160E](https://doi.org/10.1039/C8CE01160E).
- 13 K. Binnemans, Interpretation of europium(III) spectra, *Coord. Chem. Rev.*, 2015, **295**, 1–45, DOI: [10.1016/j.ccr.2015.02.015](https://doi.org/10.1016/j.ccr.2015.02.015).
- 14 Y. Xie, X. Geng, J. Guo, W. Shi, Q. Lv, J. Kong, Y. Li, B. Deng and R. Yu, Luminescence of a novel double-perovskite $\text{Sr}_2\text{InSbO}_6:\text{Eu}^{3+}$ orange-red-emitting phosphor for white LEDs and visualization of latent fingerprints, *Mater. Res. Bull.*, 2022, **146**, 111574, DOI: [10.1016/j.materresbull.2021.111574](https://doi.org/10.1016/j.materresbull.2021.111574).
- 15 M. İlhan, M. İ. Katı, L. F. Güleriyüz and S. Kılıç, Judd-Ofelt analysis and structural, morphological, optical characteristics of Eu^{3+} doped Ca_2GdMO_6 ($\text{M}=\text{Nb}$, Ta) double perovskite phosphors, *J. Lumin.*, 2025, **286**, 121361, DOI: [10.1016/j.jlumin.2025.121361](https://doi.org/10.1016/j.jlumin.2025.121361).
- 16 C. Zhou, L. Zhang, H. Sun, H. Yu, L. Guan, L. Zhang, F. Li, F. Zeng, X. Du, D. Zhang, Y. Xu and R. Yu, A novel double-perovskite structure $\text{Mg}_2\text{YVO}_6:\text{Sm}^{3+}$ phosphor with zero thermal quenching characteristics for w-LEDs and latent fingerprint development, *J. Lumin.*, 2025, **281**, 121147, DOI: [10.1016/j.jlumin.2025.121147](https://doi.org/10.1016/j.jlumin.2025.121147).
- 17 V. P. Veena, S. V. Sajith, A. M. H. Thasneem, M. Aardhra, C. K. Shilpa, S. V. Jasira and K. M. Nissamudeen, Multimodal responsive Dy^{3+} , Li^+ activated $\text{Gd}_2\text{MgTiO}_6$ phosphors for ideal wLED, potent anti-counterfeiting, fingerprint visualization, and encryption coding, *Mater. Sci. Semicond. Process.*, 2024, **179**, 108497, DOI: [10.1016/j.mssp.2024.108497](https://doi.org/10.1016/j.mssp.2024.108497).
- 18 M. İlhan, L. F. Güleriyüz, S. Gökçe and S. Kılıç, Judd-Ofelt and photoluminescence analysis of $\text{Ca}_2\text{GdSbO}_6:\text{Eu}^{3+}$ and $\text{Ca}_2\text{GdSbO}_6:\text{Eu}^{3+}$, B^{3+} phosphors for red emission performance, *Mater. Sci. Eng., B*, 2025, **322**, 118662, DOI: [10.1016/j.mseb.2025.118662](https://doi.org/10.1016/j.mseb.2025.118662).
- 19 J. Y. Park and H. K. Yang, Development of red-emitting $\text{La}_2\text{ZnTiO}_6:\text{Eu}^{3+}$ phosphors for WLED and visualization of latent fingerprint applications, *Mater. Today Commun.*, 2022, **31**, 103391, DOI: [10.1016/j.mtcomm.2022.103391](https://doi.org/10.1016/j.mtcomm.2022.103391).
- 20 X. Ouyang, R. Liu, X. Hu, J. Li, R. Tang, X. Jin, S. Chen, X. Yao, B. Deng, H. Geng and R. Yu, Preparation, characterization, and application of a red phosphor $\text{Ca}_2\text{InTaO}_6:\text{Eu}^{3+}$ in w-LEDs and latent fingerprint detection,



- J. Alloys Compd.*, 2023, **939**, 168715, DOI: [10.1016/j.jallcom.2023.168715](https://doi.org/10.1016/j.jallcom.2023.168715).
- 21 L. F. Güleriyüz and M. İlhan, Structural, morphological, spectral properties and high quantum efficiency of Eu^{3+} , B^{3+} co-activated double perovskite Ba_2GdMO_6 ($\text{M} = \text{Nb}, \text{Ta}$) phosphors, *Mater. Sci. Eng., B*, 2024, **304**, 117373, DOI: [10.1016/j.mseb.2024.117373](https://doi.org/10.1016/j.mseb.2024.117373).
- 22 T. H. Vu, D. Stefańska and P. J. Dereń, Effect of A-cation radius on the structure, luminescence, and temperature sensing of double perovskites A_2MgWO_6 doped with Dy^{3+} ($\text{A} = \text{Ca}, \text{Sr}, \text{Ba}$), *Inorg. Chem.*, 2023, **62**, 20020–20029, DOI: [10.1021/acs.inorgchem.3c02798](https://doi.org/10.1021/acs.inorgchem.3c02798).
- 23 M. İlhan and L. F. Güleriyüz, Investigation of structural, morphological and spectral characteristics of double perovskite $\text{Sr}_2\text{GdTao}_6$ phosphors doped with Eu^{3+} , and co-doped Eu^{3+} , B^{3+} having improved quantum efficiency, *J. Mater. Sci.: Mater. Electron.*, 2024, **35**, 2163, DOI: [10.1007/s10854-024-13832-6](https://doi.org/10.1007/s10854-024-13832-6).
- 24 S. W. Wi, J. W. Seo, Y. D. Lee, J. H. Choi, Y. S. Lee and J. S. Chung, Cation substitution induced structural phase transitions and luminescence properties of Eu^{3+} -doped A_2LaNbO_6 ($\text{A} = \text{Ba}, \text{Sr}, \text{and Ca}$) double perovskite, *J. Alloys Compd.*, 2024, **976**(2024), 173102, DOI: [10.1016/j.jallcom.2023.173102](https://doi.org/10.1016/j.jallcom.2023.173102).
- 25 N. Degda, N. Patel, M. Singhal, K. V. R. Murthy, N. Chauhan, V. Verma and M. Srinivas, Luminescence and dosimetry investigations of $\text{Eu}(\text{III})$ doped Ca_2CeVO_6 novel double perovskite, *Opt. Mater.*, 2024, **155**, 115861, DOI: [10.1016/j.optmat.2024.115861](https://doi.org/10.1016/j.optmat.2024.115861).
- 26 N. Degda, N. Patel, V. Verma, K. V. R. Murthy, N. Chauhan, M. Singhal and M. Srinivas, Photoluminescence and thermoluminescence kinetic features of Eu^{3+} doped Sr_2YVO_6 double perovskite phosphor, *Opt. Mater.*, 2023, **142**, 114019, DOI: [10.1016/j.optmat.2023.114019](https://doi.org/10.1016/j.optmat.2023.114019).
- 27 Y. Alsabah, A. Elden, M. Alsalthi, A. Elbadawi and M. Siddig, Structural and optical properties of A_2YVO_6 ($\text{A} = \text{Mg}, \text{Sr}$) double perovskite oxides, *Results Phys.*, 2019, **15**, 102589, DOI: [10.1016/j.rinp.2019.102589](https://doi.org/10.1016/j.rinp.2019.102589).
- 28 X. Meng, S. Huang and M. Shang, Red emitting $\text{Ba}_2\text{GdVO}_6:\text{Eu}^{3+}$ phosphors for blue light converted warm white LEDs, *Inorg. Chem. Commun.*, 2020, **113**, 107768, DOI: [10.1016/j.inoche.2020.107768](https://doi.org/10.1016/j.inoche.2020.107768).
- 29 M. Yu, J. Lin and S. B. Wang, Effects of x and R^{3+} on the luminescent properties of Eu^{3+} in nanocrystalline $\text{YV}_x\text{P}_{1-x}\text{O}_4:\text{Eu}^{3+}$ and $\text{RVO}_4:\text{Eu}^{3+}$ thin-film phosphors, *Appl. Phys. A*, 2005, **80**, 353–360, DOI: [10.1007/s00339-003-2230-5](https://doi.org/10.1007/s00339-003-2230-5).
- 30 L. Li, W. Wang, Y. Pan, Y. Zhu, X. Liu, H. M. Noh, B. K. Moon, B. C. Choib and J. H. Jeong, Preferential occupancy of Eu^{3+} and energy transfer in Eu^{3+} doped $\text{Sr}_2\text{V}_2\text{O}_7$, $\text{Sr}_9\text{Gd}(\text{VO}_4)_7$ and $\text{Sr}_2\text{V}_2\text{O}_7/\text{Sr}_9\text{Gd}(\text{VO}_4)_7$ phosphors, *RSC Adv.*, 2018, **8**, 1191–1202, DOI: [10.1039/c7ra08089a](https://doi.org/10.1039/c7ra08089a).
- 31 H. Kim, J. Kim, S. Lim and K. Park, Photoluminescence of vanadate garnet $\text{Ca}_2\text{NaMg}_{2-x}\text{V}_3\text{O}_{12}:\text{xEu}^{3+}$ phosphors synthesized by solution combustion method, *J. Nanosci. Nanotechnol.*, 2016, **16**, 1827–1830, DOI: [10.1166/jnn.2016.11969](https://doi.org/10.1166/jnn.2016.11969).
- 32 Y. Li, X. Wei, H. Chen, G. Pang, Y. Pan, L. Gong, L. Zhu, G. Zhu, Y. Ji and J. Li, A new self-activated vanadate phosphor of $\text{Na}_2\text{YMg}_2(\text{VO}_4)_3$ and luminescence properties in Eu^{3+} doped $\text{Na}_2\text{YMg}_2(\text{VO}_4)_3$, *J. Lumin.*, 2015, **168**, 124–129, DOI: [10.1016/j.jlumin.2015.08.002](https://doi.org/10.1016/j.jlumin.2015.08.002).
- 33 L. Li, Y. Pan, W. Wang, W. Zhang, Z. Wen, X. Leng, Q. Wang, L. Zhou, H. Xu, Q. Xia, L. Liu, H. Xiang and X. Liu, $\text{O}^{2-}-\text{V}^{5+}$ charge transfer band, chemical bond parameters and R/O of Eu^{3+} doped $\text{Ca}(\text{VO}_3)_2$ and $\text{Ca}_3(\text{VO}_4)_2$: A comparable study, *J. Alloys Compd.*, 2017, **726**, 121–131, DOI: [10.1016/j.jallcom.2017.07.284](https://doi.org/10.1016/j.jallcom.2017.07.284).
- 34 P. L. Hu, X. Guo, J. Hu, C. Deng and R. Cui, Anomalous $^5\text{D}_0 \rightarrow ^7\text{F}_4$ transition of Eu^{3+} -doped BaLaGaO_4 phosphors for WLEDs and plant growth applications, *Adv. Opt. Mater.*, 2024, **12**, 2301760, DOI: [10.1002/adom.202301760](https://doi.org/10.1002/adom.202301760).
- 35 A. T. Schwarz, M. Ströbele, D. Enseling, T. Jüstel and H. J. Meyer, Synthesis, Structure, and Eu^{3+} -Activated photoluminescence of the mixed-anion carbodiimide $\text{NaLa}_2\text{F}_3(\text{CN}_2)_2$, *Z. Anorg. Allg. Chem.*, 2025, DOI: [10.1002/zaac.202500221](https://doi.org/10.1002/zaac.202500221).
- 36 R. Skaudzius, A. Katelnikovas, D. Enseling, A. Kareiva and T. Jüstel, Dependence of the $^5\text{D}_0 \rightarrow ^7\text{F}_4$ transitions of Eu^{3+} on the local environment in phosphates and garnets, *J. Lumin.*, 2014, **147**, 290–294, DOI: [10.1016/j.jlumin.2013.11.051](https://doi.org/10.1016/j.jlumin.2013.11.051).
- 37 B. R. Judd, Optical absorption intensities of rare-earth ions, *Phys. Rev.*, 1962, **127**, 750, DOI: [10.1103/PhysRev.127.750](https://doi.org/10.1103/PhysRev.127.750).
- 38 G. S. Ofelt, Intensities of crystal spectra of rare-earth ions, *J. Chem. Phys.*, 1962, **37**, 511, DOI: [10.1063/1.1701366](https://doi.org/10.1063/1.1701366).
- 39 J. Tian, C. Zhang, Q. Fan, H. Su, Z. Chen and G. Ren, Eu^{3+} ion probe and Judd-Ofelt theory: A computational approach to determine Er^{3+} parameters in $\text{NaGd}_x\text{Yb}_{1-x}\text{F}_4$ nanomaterials, *Phys. B*, 2025, **726**, 418256, DOI: [10.1016/j.physb.2026.418256](https://doi.org/10.1016/j.physb.2026.418256).
- 40 S. A. Oommen, A. Gopinath, P. B. Gayathri, C. Joseph and P. R. Biju, Optical characteristics and Judd-Ofelt analysis of novel $\text{Ba}_3\text{Sr}_{(1-x)}\text{Nb}_2\text{O}_9:\text{xEu}^{3+}$ phosphors for luminescent applications, *J. Lumin.*, 2025, **288**, 121581, DOI: [10.1016/j.jlumin.2025.121581](https://doi.org/10.1016/j.jlumin.2025.121581).
- 41 R. Raji, P. S. Anjana and N. Gopakumar, Dual mode non-contact optical thermometry and temperature-dependent Judd-Ofelt analysis of Eu^{3+} doped $\text{LiCa}_2\text{Mg}_2\text{V}_3\text{O}_{12}$ phosphors, *Mater. Sci. Eng., B*, 2026, **323**, 118761, DOI: [10.1016/j.mseb.2025.118761](https://doi.org/10.1016/j.mseb.2025.118761).
- 42 R. Kajal, D. Singh, R. Jangra, P. Kumar, V. Kumar, H. Kumar and R. Kumar, Structural and photophysical investigation of gadolinium based Eu^{3+} doped Gd_3GaO_6 phosphor: A red emitter with high color purity for WLEDs application, *J. Alloys Compd.*, 2026, **1050**, 185688, DOI: [10.1016/j.jallcom.2025.185688](https://doi.org/10.1016/j.jallcom.2025.185688).
- 43 P. Kumar, D. Singh, S. Kadyan, H. Kumar and R. Kumar, Comprehensive investigation of $\text{Y}_2\text{Si}_2\text{O}_7:\text{Eu}^{3+}$ nanophosphors for w-LEDs: Structural, Judd-Ofelt calculation and photoluminescent characteristic with high color purity and thermal stability, *Ceram. Int.*, 2024, **50**, 34596–34608, DOI: [10.1016/j.ceramint.2024.06.267](https://doi.org/10.1016/j.ceramint.2024.06.267).



- 44 M. İlhan, M. K. Ekmekçi and İ. Ç. Keskin, Judd–Ofelt parameters and X-ray irradiation results of $\text{MNb}_2\text{O}_6:\text{Eu}^{3+}$ ($\text{M} = \text{Sr}, \text{Cd}, \text{Ni}$) phosphors synthesized via a molten salt method, *RSC Adv.*, 2021, **11**, 10451–10462, DOI: [10.1039/d0ra10834k](https://doi.org/10.1039/d0ra10834k).
- 45 M. İlhan and L. F. Güleriyüz, Boron doping effect on the structural, spectral properties and charge transfer mechanism of orthorhombic tungsten bronze $\beta\text{-SrTa}_2\text{O}_6:\text{Eu}^{3+}$ phosphor, *RSC Adv.*, 2023, **13**, 12375, DOI: [10.1039/D3RA00618B](https://doi.org/10.1039/D3RA00618B).
- 46 M. İlhan, L. F. Güleriyüz and M. İ. Katı, Study on structural, morphological, and spectral properties of $\text{LiMPO}_4:\text{Eu}^{3+}, \text{B}^{3+}$ ($\text{M} = \text{Zn}, \text{Sr}$) phosphors and latent fingerprint applications, *Mater. Sci. Eng., B*, 2025, **316**, 118124, DOI: [10.1016/j.mseb.2025.118124](https://doi.org/10.1016/j.mseb.2025.118124).
- 47 A. Pimpalkar, S. Dhale, N. Ugemuge, A. Mistry, R. B. Joshi, S. Khapre, M. Patwardhan and K. Raulkar, Spectroscopic properties and Judd–Ofelt analysis of $\text{Ca}_2\text{La}_3(\text{SiO}_4)_3\text{F}:\text{Eu}^{3+}$ phosphor, *J. Electron. Mater.*, 2025, **54**, 3024–3034, DOI: [10.1007/s11664-025-11824-8](https://doi.org/10.1007/s11664-025-11824-8).
- 48 M. İlhan and İ. Ç. Keskin, Evaluation of structural behaviour, radioluminescence, Judd–Ofelt analysis and thermoluminescence kinetic parameters of Eu^{3+} doped TTB–type lead metaniobate phosphor, *Phys. B*, 2020, **585**, 412106, DOI: [10.1016/j.physb.2020.412106](https://doi.org/10.1016/j.physb.2020.412106).
- 49 A. Pimpalkar, N. Ugemuge, A. A. Mistry, S. Dhale, R. B. Joshi, S. A. Khapre, M. Patwardhan, R. Nithya, K. Greeshma and K. M. Nissamudeen, Fluorescence spectra and optical transition properties of Eu^{3+} -Doped $\text{Ca}_3\text{NbGa}_3\text{Si}_2\text{O}_{14}$ phosphor, *J. Electron. Mater.*, 2025, **54**, 2264–2274, DOI: [10.1007/s11664-024-11674-w](https://doi.org/10.1007/s11664-024-11674-w).
- 50 E. Muthulakshmi, K. J. Albert and S. M. M. Kennedy, Judd–Ofelt calculation and photoluminescence properties of europium doped $\text{KCaBi}(\text{PO}_4)_2$ phosphors for solid state lighting devices, *Mater. Res. Bull.*, 2025, **192**, 113638, DOI: [10.1016/j.materresbull.2025.113638](https://doi.org/10.1016/j.materresbull.2025.113638).
- 51 B. Verma, R. N. Baghel, D. P. Bisen, N. Brahme and V. Jena, Microstructural, luminescence properties and Judd–Ofelt analysis of Eu^{3+} activated $\text{K}_2\text{Zr}(\text{PO}_4)_2$ phosphor for lighting and display applications, *Opt. Mater.*, 2022, **129**, 112459, DOI: [10.1016/j.optmat.2022.112459](https://doi.org/10.1016/j.optmat.2022.112459).
- 52 M. Zikriya, C. G. Renuka and C. Manjunath, Optical absorption intensity analysis using Judd–Ofelt theory and photoluminescence investigation for red-emitting $\text{Eu}^{3+}:\text{TiO}_2$ nanoparticles, *Solid State Sci.*, 2020, **107**, 106371, DOI: [10.1016/j.solidstatesciences.2020.106371](https://doi.org/10.1016/j.solidstatesciences.2020.106371).
- 53 B. Verma, R. N. Baghel, D. P. Bisen, N. Brahme and V. Jena, Judd–Ofelt analysis and luminescent characterization of Eu^{3+} activated $\text{Li}_2\text{Zr}(\text{PO}_4)_2$ phosphor, *Opt. Mater.*, 2021, **118**, 111196, DOI: [10.1016/j.optmat.2021.111196](https://doi.org/10.1016/j.optmat.2021.111196).
- 54 M. İlhan, L. F. Güleriyüz and M. İ. Katı, Exploring the effect of boron on the grain morphology change and spectral properties of Eu^{3+} activated barium tantalate phosphor, *RSC Adv.*, 2024, **14**, 2687–2696, DOI: [10.1039/d3ra08197d](https://doi.org/10.1039/d3ra08197d).
- 55 M. İlhan, L. F. Güleriyüz, S. Gökçe and H. Demirer, Comparative luminescence and Judd–Ofelt analysis of Eu^{3+} -doped Ca_2GdVO_6 and Sr_2GdVO_6 phosphors for red-emitting applications, *Mater. Sci. Eng., B*, 2026, **322**, 118761, DOI: [10.1016/j.mseb.2025.118776](https://doi.org/10.1016/j.mseb.2025.118776).
- 56 C. Manjunath, M. S. Rudresha, R. H. Krishna, B. M. Nagabhushana, B. M. Walsh, K. R. Nagabhushana and B. S. Panigrahi, Spectroscopic studies of strong red emitting $\text{Sr}_2\text{SiO}_4:\text{Eu}^{3+}$ nanophosphors with high color purity for application in WLED using Judd–Ofelt theory and TL glow curve analysis, *Opt. Mater.*, 2018, **85**, 363–372, DOI: [10.1016/j.optmat.2018.08.070](https://doi.org/10.1016/j.optmat.2018.08.070).
- 57 N. T. Q. Lien, T. T. Hong, P. V. Do and H. V. Tuye, Influence of dopant concentration on raman spectra and Judd–Ofelt intensity parameters of red-emitting Eu^{3+} -doped $\text{Sr}_2\text{MgSi}_2\text{O}_7$, *Opt. Mater.*, 2025, **160**, 116754, DOI: [10.1016/j.optmat.2025.116754](https://doi.org/10.1016/j.optmat.2025.116754).
- 58 P. Khajuria, V. D. Sharma, I. Kumar, A. Khajuria, R. Prakash and R. J. Choudhary, Optoelectronic properties of $\text{Na}_2\text{ZrO}_3:\text{Eu}^{3+}$ phosphor: Judd–Ofelt insights and applications in solid-state lighting and latent fingerprinting, *J. Alloys Compd.*, 2025, **1025**, 180268, DOI: [10.1016/j.jallcom.2025.180268](https://doi.org/10.1016/j.jallcom.2025.180268).
- 59 V. D. Sharma, P. Khajuria, A. Khajuria, R. Prakash and R. J. Choudhary, Photoluminescent and X-ray photoemission studies of Eu^{3+} -doped kosnarite $\text{KZr}_2(\text{PO}_4)_3$ nanophosphor and its Judd–Ofelt analysis, *J. Nanopart. Res.*, 2024, **26**, 166, DOI: [10.1007/s11051-024-06073-5](https://doi.org/10.1007/s11051-024-06073-5).
- 60 R. Gopal and J. Maram, The photoluminescence and Judd–Ofelt investigations of UV, near-UV and blue excited highly pure red emitting $\text{BaWO}_4:\text{Eu}^{3+}$ phosphor for solid state lighting, *Ceram. Int.*, 2023, **49**, 28118–28129, DOI: [10.1016/j.ceramint.2023.06.063](https://doi.org/10.1016/j.ceramint.2023.06.063).
- 61 M. İlhan, M. K. Ekmekçi and L. F. Güleriyüz, Effect of boron incorporation on the structural, morphological, and spectral properties of $\text{CdNb}_2\text{O}_6:\text{Dy}^{3+}$ phosphor synthesized by molten salt process, *Mater. Sci. Eng., B*, 2023, **298**, 116858, DOI: [10.1016/j.mseb.2023.116858](https://doi.org/10.1016/j.mseb.2023.116858).
- 62 V. A. Raj, V. R. Mala, S. M. M. Kennedy and H. G. Evangeline, DFT calculation, optical, photoluminescent, and radiative (Judd–Ofelt) properties of phosphate based red emitting $\text{Na}_2\text{SrMg}(\text{PO}_4)_2:\text{Eu}^{3+}$ phosphor for solid state lighting, *Opt. Mater.*, 2025, **168**, 117418, DOI: [10.1016/j.optmat.2025.117418](https://doi.org/10.1016/j.optmat.2025.117418).
- 63 V. Rathina Mala, S. M. M. Kennedy, A. Princy and K. J. Albert, Photoluminescence emission enhancement in the $\text{LiSrVO}_4:\text{Eu}^{3+}$ vanadate phosphor by partial substitution of M^+ ions ($\text{M}^+=\text{Li}^+/\text{Na}^+/\text{K}^+$); optical thermometry; and optical transition probabilities using, Judd–Ofelt analysis, *J. Lumin.*, 2024, **275**, 120778, DOI: [10.1016/j.jlumin.2024.120778](https://doi.org/10.1016/j.jlumin.2024.120778).
- 64 G. V. Kanmani, V. Ponnusamy, G. Rajkumar and S. M. M. Kennedy, A new Milarite type $\text{KMLS}:\text{Eu}^{3+}$ orange-red-emitting phosphor for pc-white LEDs and Forensic applications, *Ceram. Int.*, 2024, **50**, 2523–2540, DOI: [10.1016/j.ceramint.2023.05.171](https://doi.org/10.1016/j.ceramint.2023.05.171).
- 65 S. Miao, R. Shi, Y. Zhang, D. Chen and Y. Liang, Deep-red $\text{Ca}_3\text{Al}_2\text{Ge}_3\text{O}_{12}:\text{Eu}^{3+}$ garnet phosphor with near-unity internal quantum efficiency and high thermal stability for



- plant growth application, *Adv. Mater. Technol.*, 2023, **8**, 2202103, DOI: [10.1002/admt.202202103](https://doi.org/10.1002/admt.202202103).
- 66 H. Guo, X. Huang and Y. Zeng, Synthesis and photoluminescence properties of novel highly thermalstable red-emitting $\text{Na}_3\text{Sc}_2(\text{PO}_4)_3:\text{Eu}^{3+}$ phosphors for UV-excited white-light-emitting diodes, *J. Alloys Compd.*, 2018, **741**, 300–306, DOI: [10.1016/j.jallcom.2017.12.316](https://doi.org/10.1016/j.jallcom.2017.12.316).
- 67 W. Wang, Z. Li, K. Wu, Y. Wang and Q. Liu, Synthesis, structure, and luminescence properties of $\text{Y}_2(\text{MoO}_4)_3:\text{Eu}^{3+}$ red phosphors for white light emitting diodes, *J. Alloys Compd.*, 2025, **1019**, 179327, DOI: [10.1016/j.jallcom.2025.179327](https://doi.org/10.1016/j.jallcom.2025.179327).
- 68 S. Wang, Q. Sun, B. Devakumar, J. Liang, L. Sun and X. Huang, Novel high color-purity Eu^{3+} -activated $\text{Ba}_3\text{Lu}_4\text{O}_9$ red-emitting phosphors with high quantum efficiency and good thermal stability for warm white LEDs, *J. Lumin.*, 2019, **209**, 156–162, DOI: [10.1016/j.jlumin.2019.01.050](https://doi.org/10.1016/j.jlumin.2019.01.050).
- 69 Z. Zhang, L. Sun, B. Devakumar, J. Liang, S. Wang, Q. Sun, S. J. Dhoble and X. Huang, Novel highly luminescent double-perovskite $\text{Ca}_2\text{GdSbO}_6:\text{Eu}^{3+}$ red phosphors with high color purity for white LEDs: Synthesis, crystal structure, and photoluminescence properties, *J. Lumin.*, 2020, **221**, 117105, DOI: [10.1016/j.jlumin.2020.117105](https://doi.org/10.1016/j.jlumin.2020.117105).
- 70 Z. Zhang, W. Li, N. Ma and X. Huang, High-brightness red-emitting double-perovskite phosphor $\text{Sr}_2\text{LaTaO}_6:\text{Eu}^{3+}$ with high color purity and thermal stability, *Chin. Opt Lett.*, 2021, **19**, 030003, DOI: [10.3788/COL202119.030003](https://doi.org/10.3788/COL202119.030003).
- 71 L. F. Güleriyüz and M. İlhan, Enhancing luminescence efficiency and optical gain of $\text{Ca}_2\text{GdMO}_6:\text{Eu}^{3+}$ ($\text{M}=\text{Nb}$, Ta) phosphors via B^{3+} co-doping for forensic imaging applications, *Ceram. Int.*, 2025, **51**, 63280–63295, DOI: [10.1016/j.ceramint.2025.11.111](https://doi.org/10.1016/j.ceramint.2025.11.111).
- 72 K. Thomas, D. Alexander, K. P. Mani, S. Gopi, S. A. Kumar, P. R. Biju, N. V. Unnikrishnan and C. Joseph, Intrinsic red luminescence of Eu^{3+} -activated lanthanum molybdate: Insights into the spectroscopic features using Judd–Ofelt theoretical analysis, *J. Phys. Chem. Solids*, 2020, **137**, 109212, DOI: [10.1016/j.jpcs.2019.109212](https://doi.org/10.1016/j.jpcs.2019.109212).
- 73 M. İ. Katı, S. Gökçe, İ. Ç. Keskin, M. Türemis, A. Çetin and R. Kibar, Luminescence characteristics and kinetic parameters of $\text{LiBaPO}_4:\text{Tb}^{3+}$, Dy^{3+} phosphors synthesized by sol-gel method, *J. Lumin.*, 2024, **266**, 120312, DOI: [10.1016/j.jlumin.2023.120312](https://doi.org/10.1016/j.jlumin.2023.120312).
- 74 L. F. Güleriyüz, Assessing of photoluminescence and structural properties of Dy^{+3} doped cadmium tantalate phosphor on the basis of charge balance, *Hacettepe J. Biol. Chem.*, 2022, **50**, 247–254, DOI: [10.15671/hjbc.1056363](https://doi.org/10.15671/hjbc.1056363).
- 75 C. S. McCamy, Correlated color temperature as an explicit function of chromaticity coordinates, *Color Res. Appl.*, 1992, **17**, 142–144, DOI: [10.1002/col.5080170211](https://doi.org/10.1002/col.5080170211).

